



# A new fast and efficient dehazing and defogging algorithm for single remote sensing images

Apurva Kumari\*, Subhendu Kumar Sahoo

*Department of Electronics and Communication Engineering, B V Raju Institute of Technology, Narsapur, Hyderabad, India*

*Department of Electrical and Electronics Engineering, Birla Institute of Technology and Science-Pilani, Hyderabad, India*



## ARTICLE INFO

**Keywords:**

Remote sensing  
Atmospheric light  
Transmission map  
Performance metrics

## ABSTRACT

Information about the earth's surface is difficult to capture in remote sensing images because bad weather greatly curtails visibility and diminishes visual contrast in the images. For the purpose of military survey and aerial surveillance, these images are crucial for providing information. It is quintessential to eradicate bad weather conditions like haze and fog from remote sensing images. Recently, numerous deweathering initiatives and endeavors have been undertaken to alleviate these limitations. These contemporary deweathering approaches, however, are inadequate to recover dense haze images. This work presented a novel visibility restoration approach based on segmentation and unsharp mask guided filtering method. It consists of the following steps to restore the scene's radiance: First, a segmentation method is employed to determine atmospheric light to quantify contrast and color. Estimation of the transmission map utilizing the dark channel prior is then performed to precisely determine the proximity between objects. The resultant output image contains halo artifacts and inconsistencies in the structure. A guided filter method based on unsharp masking is employed to optimize the transmission map in order to solve this issue. The experimental results demonstrate that the proposed indicators ensures high uniformity regarding qualitative and quantitative evaluation using six performance metrics: mean square error (MSE), peak signal-to-noise ratio (PSNR), structural similarity index measure (SSIM), universal image quality index (UQI), fog-aware density evaluator (FADE), dehazing algorithm index (DHQI), standard deviation (CC), and blind contrast enhancement assessment ( $e$  and  $r$ ).

## 1. Introduction

Remote sensing images provide information that is useful in a wide range of fields, including meteorology, resource exploration, military activities, and many more. However, atmospheric circumstances like haze and fog reduced contrast and color in the captured natural and remote sensing images, resulting in low visibility [1–3]. Generally, dehazing is a technique used to visually improve visibility, which has been negatively impacted by atmospheric conditions when horizontal visibility at ground level is greater than 1 km. The defogging method is similar to that of haze removal, but it concentrates on fog, which, in comparison with haze, is a cloud of water droplets close to the ground that reduces horizontal visibility to less than 1 km. Because light is deflected and absorbed by air particles during bad weather, dehazing and defogging are both included in the algorithms to improve visibility. In order to improve an image that has been degraded by rain streaks and buildup, single-image de-raining attempts to restore the rain-free background scenes. Rain and haze have different characteristics; rain occurs during dynamic severe weather, whereas haze and fog occur

during static bad weather. The size of the water droplets in a dynamic condition is more than 1000 times larger than in a static condition. In this study, hazy and foggy weather conditions were taken into account for dehazing and defogging the remote sensing images.

The physical depictions of natural and remote sensing images differ in the following manner: First, the natural image is typically obtained by directing the camera to a distance where the contrast and color saturation of the image deteriorate with increasing scene depth. The transmission map for natural images can be derived using several priors [4–7], and [8] according to this characteristic. However, remote sensing images frequently show less variation in contrast and color saturation than natural images because they are captured by remote optical sensors on satellites. Second, with a few notable exceptions, ambient light is frequently calculated arbitrarily or determined by the pixel with the greatest hazy opacity [5,9,10]. The term “haze-opaque region” typically refers to the sky area in natural images. Third, despite natural images, which frequently have identical resolution and scale, remote sensing images frequently track a wide range

\* Corresponding author at: B V Raju Institute of Technology, Narsapur, Telangana, 502313, India.

E-mail address: [kumari.apurva198@gmail.com](mailto:kumari.apurva198@gmail.com) (A. Kumari).

of spatial resolutions, scales, and shapes of objects on the earth's surface. Consequently, hazes typically vary in remote sensing images. Therefore, natural envision dehazing techniques that were created for an elementary instance are unable to effectively remove hazes from remote sensing images. These distinctions jeopardize the efficiency of a natural image when used for remote sensing. These discrepancies must be addressed in order for them to realize their full potential. As a result, for considerable improvements in the visibility of restored remote sensing images, an effective dehazing and defogging method is required.

In recent years, researchers have investigated the removal of haze and fog from satellite imagery. Few researchers have been presented enhancement-based methods for dehazing [11–14]. It takes less time to compute and implement the histogram equalization approach [15]. As a result, this approach can handle high-resolution remote sensing data. However, since the characteristics of overall contrast enhancement, this method is only suitable for strong haze for dehazing. Kim et al. [16,17] proposed a local histogram equalization method for dehazing to address this issue. Shi et al. [18] suggested a method for restoring hazy images based on the Retinex algorithm and chromaticity. The (URSHR) Urban technique was developed by Huang et al. [19] for dehazing remote sensing images. A framework for image restoration and haze removal was presented by Chaudhry et al. [20]. These approaches are straightforward and effective in restoring dehazy images. The images that result, however, show halos and artifacts.

Recently, Physical model-based dehazing techniques have gained popularity. These models go through a series of stages to dehaze remote sensing images. As depth uncertainty is a poorly articulated issue, first calculate the transmission depth. The next step is to evaluate the atmospheric light. Finally, restore the haze and fog free images. He et al. [4] presented a dark channel prior (DCP) method for dehazing. It comes from the observation that by solving the Physics-based model, most local areas of a haze-free image generally provide high-quality images. Tan [9] proposed the method based on the maximizing contrast enhancement concept to dehaze the images. However, the recovered images are suffered from the halos and color over-saturation. Fattal [5] estimated the albedo using the independent component analysis approach. In [21], the dehazing procedure is simplified based on the blocking phenomena, which has negligible impact on dehazed images. For remote sensing images, Zheng et al. [22] introduced a threshold-based technique to ignore the influence of bright objects. In [23], for refinement of transmission map median filter method is used. For remotely sensed multispectral images, Wang et al. [24] devised a blockbased DCP approach. Dai et al. [25] were able to determine the each pixel's three channels, at the very least by using the dark channel approach of remote sensing images. In [6] presented a non-local dehazing technique based on K-means [26] to cluster into haze-lines [10] for estimation of the transmission map. The color attenuation prior (CAP) method for restoring the depth information effectively and recover the scene radiance presented in [27]. In [28], proposed a method based on haze thickness map for dehazing the remote sensing images.

Latest developments in physical-based frameworks and dark-object subtraction strategies have been used to dehaze multispectral data and single image data [29–36]. Pan et al. [29] proposed a deformed haze imaging model (DHIM) to dehaze multispectral remote sensing data. The haze-free multispectral data was also recovered using the adaptive dehazing method namely dark channel-saturation prior method [31]. To remove haze from remote sensing images, IDeRS [33], method introduced.

Deep learning techniques are constantly improving, and the usefulness of convolution neural network (CNN) methods has been demonstrated in a wide range of applications such as segmentation and image dehazing [37–41]. Cai et al. [42] proposed a CNN-based methodology to dehaze the transmission map by regressing it. For the dehazing, Ren et al. [43] presented a multi-scale CNN. Li et al. [44] presented an AOD-Net approach to address this problem. A gated context pooling network

with an end-to-end architecture was given in [45] to reconstitute the images. In [46], the transmission map was computed directly to restore the scene radiance using a multilayer perceptron. A structure-guided 0-norm filter is used as an additional refinement in Shin et al. [47] optimization based dehazing algorithm, which integrates the components of reflectance and radiance. A method using CNN and the underlying structure for dehazing the images was proposed by Qin et al. [48]. However, these methods necessitate larger training datasets and more processing consumption. A methodology using enhancement techniques to eliminate possible shortcomings based on deep learning methods was proposed in [49,50].

To validate state-of-the-art methods, different datasets are available for remote sensing image dehazing [51–53]. Different datasets for remote sensing image dehazing have been made accessible to validate the state-of-the-art methodologies [51–53]. Recently, Deep learning algorithms have been used in conjunction with feature extraction to dehaze remote-sensing images [8,54–58]. These strategies yielded statistically acceptable results. However, artifacts were still evident in the restored output. The most recent dehazing methods for remote sensing images hinge on restoration and enhancement techniques [7,59–65]. As illustrated in Fig. 1, different defogging remote sensing images are restored using several popular methods. However, the limitations of these approaches include color distortions. In accordance with suggestions presented in [66,67], and [68] based on the “Overcoming nonlinear dynamics in diabetic retinopathy classification: A robust AI-based model with chaotic swarm intelligence optimization and recurrent long short-term memory; Artificial intelligence-based robust hybrid algorithm design and implementation for real-time detection of plant diseases in agricultural environments; Detection of solder paste defects with an optimization-based deep learning model using image processing techniques” show the efficacy as well as the resilience of the method by employing an idea of image processing methods.

The present work introduces segmentation and unsharp mask guided filtering for dehazing remote sensing images. First, threshold-based approaches were employed to calculate atmospheric light. Second, transmission maps for natural and remote sensing image hazes can be described using the same mathematical methods despite the fact that their underlying causes differ. The “optical depth” of the scenes in an image is actually what they are all exponential to. This suggests that remote sensing can also use the transmission map model of natural images but with a different interpretation, which will be discussed in Section 3. Third, the transmission map can be estimated by using an unsharp-masking guiding filter. Due to its ability to progressively eliminate haze at various scales, this process is particularly effective for remote sensing images.

In this paper, a novel haze removal algorithm is proposed for dehazing the remote sensing images. The main contributions of this study are summarized as follows:

- (1) Contrary to the various approaches available for the atmospheric light estimation, consider the highest pixel intensity; the proposed methodology utilizes threshold based techniques for atmospheric light selection.

- (2) For the transmission map estimation, the dark channel method provides appreciable results, but is still plagued with artifacts. Furthermore, unlike bilateral and guided filtering, the proposed method does not have a gradient reversal effect. Unsharp mask guided filtering is introduced into the physical model to refine the transmission map and gradually eliminate haze from remote sensing images.

- (3) The proposed methodology's accomplishment on the simulated images enables better results in both the quantitative and qualitative domains.

The structure of this paper is as follows. The background and associated algorithm are covered in Section 2. Section 3 outlines in detail our proposed fog and haze removal approach. Performance measurements, comparisons, and experimental findings are presented in Sections 4 and 5. Here, the proposed algorithm's performance is evaluated with that of previous most recent techniques. Sections 6 and 7 present the discussion and application areas for enhancing visibility. Section 8 finally presents the conclusion.

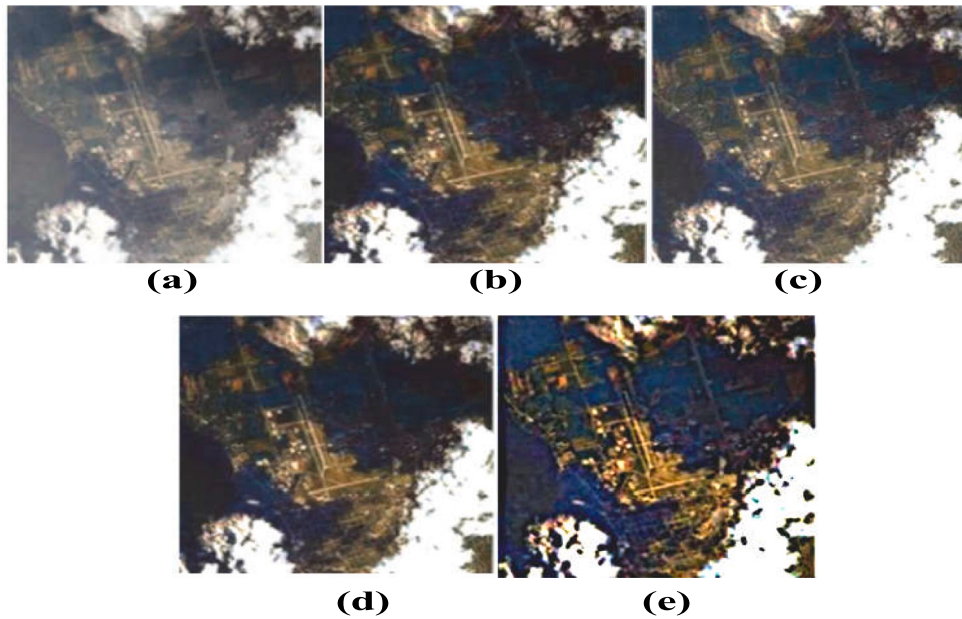


Fig. 1. Dehazing remote sensing results of various approaches: (a) Original image. (b) DCP [20]. (c) Liu et al. [28]. (d) Qin et al. [47]. (e) Our method.

## 2. Background and related work

### 2.1. Atmospheric scattering model

The majority of dehazing algorithms in computer vision and computer graphics are based on the Nayar et al. [15,16] degradation model. The following is a widely used approach for image formation in the presence of bad weather:

$$I_i(x) = J_{ri}(x)t(x) + A_l(1 - t(x)) \quad (1)$$

where,  $I_i(x)$  is the captured input image,  $J_{ri}(x)$  is the restored image,  $A_l$  is the atmospheric light, and  $t$  is the transmission map. It refers to the quantity of light that enters the camera uninterrupted. Restoration of  $J_{ri}(x)$ ,  $A_l$  and  $t$  from  $I_i(x)$  is required in order to remove haze from images. Take into account that there are  $4N + 3$  unknowns,  $3N$  constraints, for an  $N$ -pixel RGB image  $I_i(x)$ . The properties of the recovered image are the unknown parameters that must be accessed in order to obtain a dehazing image. The light beam from an object is attenuated by the presence of atmospheric particles. This is known as attenuation and primary cause to reduce the contrast in the captured images. This is referred to as attenuation, and it is the key reason why the contrast in the captured images is curtailed. The direct attenuation of illumination from the object's surface is represented by the first term,  $J_{ri}(x)t(x)$ . The light from the environmental source is highly scattered and reaches towards the camera and adds whiteness in the captured images. Airlight is the term used to describe this phenomenon.  $A_l(1 - t(x))$  is being used to signify the term "airlight". If the atmosphere is assumed to be homogeneous, the transmission  $t(x)$  can be expressed as:

$$t(x) = e^{-\beta d_{sd}(x)} \quad (2)$$

where,  $\beta$  is the atmosphere's scattering coefficient and  $d_{sd}(x)$  stands for the scene's depth. The transmission map exhibits exponential attenuation with scene depth  $d_{sd}(x)$ , as illustrated by this equation. Eq. (2) means that the transmission  $t(x, y)$  when the haze model equation is geometrically seen in the three color space (R, G, and B):

$$t(x) = \frac{\|A_l - I_i(x)\|}{\|A_l - J_{ri}(x)\|} = \frac{A_l^c - I_i(x)^c(x)}{A_l^c - J_{ri}(x)^c(x)} \quad (3)$$

where the color channel index is  $c \in \{r, g, b\}$ .

The accurate assessment of  $A_l$  and  $t(x)$  from the input image  $I_i(x)$  is required to recover the scene radiance  $J_{ri}(x)$  from the atmospheric scattering model. The scene  $J_{ri}(x)$  can be restored once the atmospheric light and transmission have been estimated. According to the dark channel, shadows and dark objects are mostly responsible for the least intensity, which is near to zero. It comprises of the following:

$$J_{ri}^{dark}(x) = \min_{y \in \Omega(x)} (\min_{c \in \{r, g, b\}} (J_{ri}^c(y))) = 0 \quad (4)$$

Given that  $A_l^c$  has always been positive, this results in

$$J_{ri}^{dark}(x) = \min_{y \in \Omega(x)} (\min_{c \in \{r, g, b\}} (\frac{J_{ri}^c(y)}{A_l^c})) = 0 \quad (5)$$

The transmission map that will be directly estimated is as follows:

$$\tilde{t}(x, y) = 1 - w \min_c (\min_{(y) \in \Omega(x)} (\frac{I_i^c(y)}{A_l^c})) \quad (6)$$

where the initial transmission map is represented by  $\tilde{t}(x, y)$ . There are numerous significant artifacts.

### 2.2. Guided filtering approach

This filtering approach has shown better performance in speed and accuracy as compared with others filtering approaches. It assumes that the filter output image  $\hat{L}$  is a linear transform of the guidance image  $F$  at a window  $w_k$  centered at pixel  $k$ :

$$\hat{L}_i = a_k F_i + b_k \quad (7)$$

There, constants  $a_k$  and  $b_k$  are used. To determine their values, solve for:

$$E(a_k, b_k) = \sum_{i \in w_k} ((a_k F_i + b_k - L_i)^2 + \epsilon a_k^2) \quad (8)$$

Here, large values for  $a_k$  are compensated in this case by the regularization parameter epsilon. The following formula is used to calculate the optimal values of  $a_k$  and  $b_k$ :

$$a_k = \frac{\frac{1}{|w|} \sum_{i \in w_k} L_i F_i - \bar{L}_k \bar{F}_k}{\sigma_k^2 + \epsilon} \quad (9)$$

$$b_k = \bar{L}_k - a_k \bar{F}_k \quad (10)$$

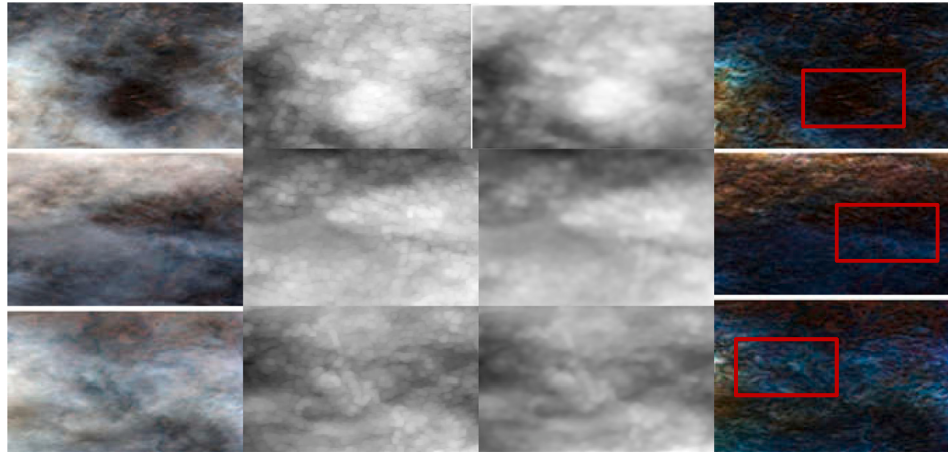


Fig. 2. Dehazing remote sensing results of various approaches: (a) Foggy image. (b) Transmission map (c) Refined Transmission map (d) Defogging image.

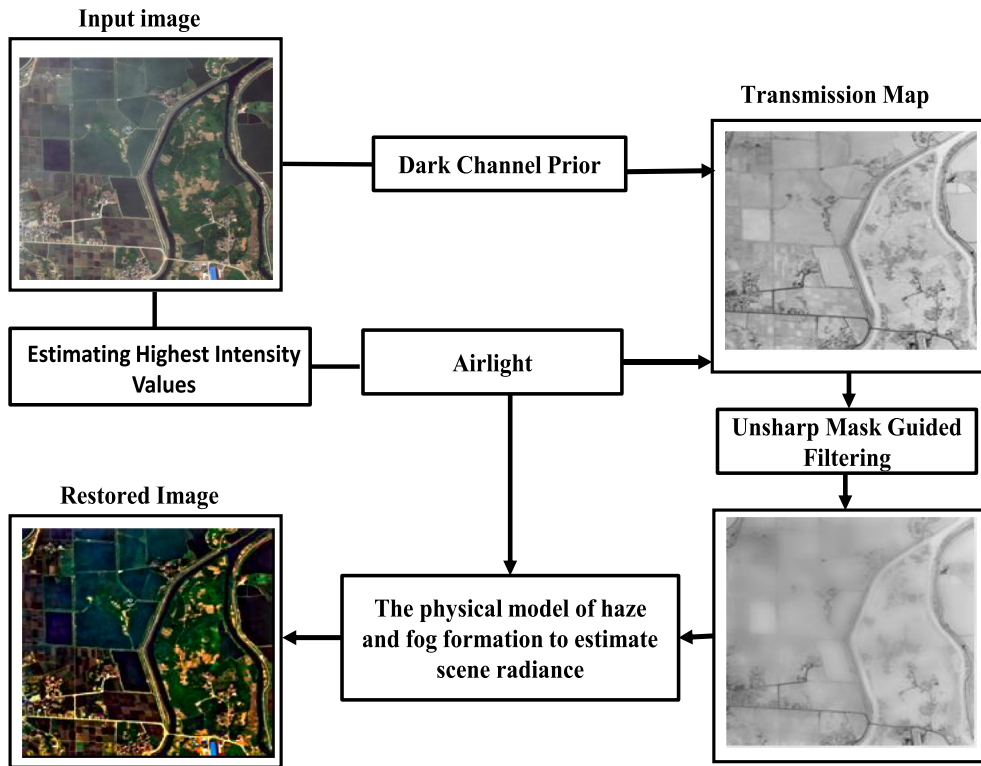


Fig. 3. Flowchart of the proposed approach.

### 3. The proposed algorithm

$$W_k(F) = \frac{1}{|w|^2} \sum_{k:(i,j) \in w_k} \left( 1 + \frac{(F_i - \mu_k)(F_j - \mu_k)}{\sigma_k^2 + \epsilon} \right) \quad (11)$$

Here,  $\mu_k$  and  $\sigma_k^2$  are the mean and variance of  $F$  in  $w_k$ , and  $|w|$  is the number of pixels in  $w_k$ . The transmission map that has been further tuned using the guided filter is as follows:

$$T_i = \sum_j W_k(F) \tilde{t}(x, y) \quad (12)$$

Although this filter has the ability to smooth edges, it nevertheless exhibits the distortions which can be seen in Figs. 2(c) and 2(d).

The proposed deweathering framework for remote sensing images is composed of the following steps: estimating the highest pixel intensity values to calculate atmospheric light; dark channel prior estimation of the initial transmission map; smoothing the transmission map inspired by enhancement techniques; and finally, scene restoration, as illustrated in Fig. 3. In the first step, the pixel intensity values are extracted using thresholding method from the weather degraded images. The brightest pixel intensity values should be found to estimate atmospheric light during the thresholding process. The next step is to assess the transmission map for further processing. The unsharp masking guided filter refines the transmission map that contains halo artifacts. Finally, restore the scene radiance using an improved transmission map and

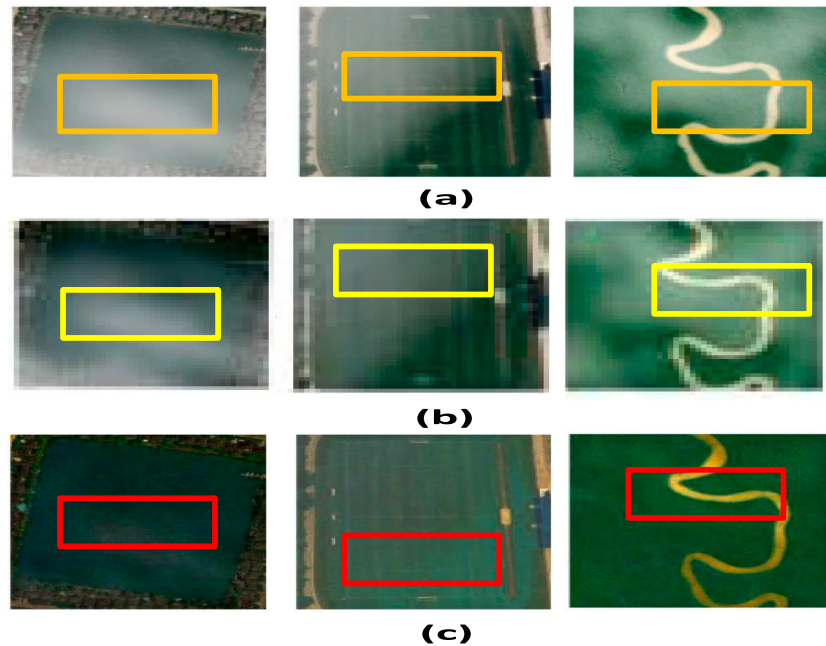


**Fig. 4.** Dehazing remote sensing results of various approaches: (a) image's densest haze (b) He et al. method [4] (c) proposed method.

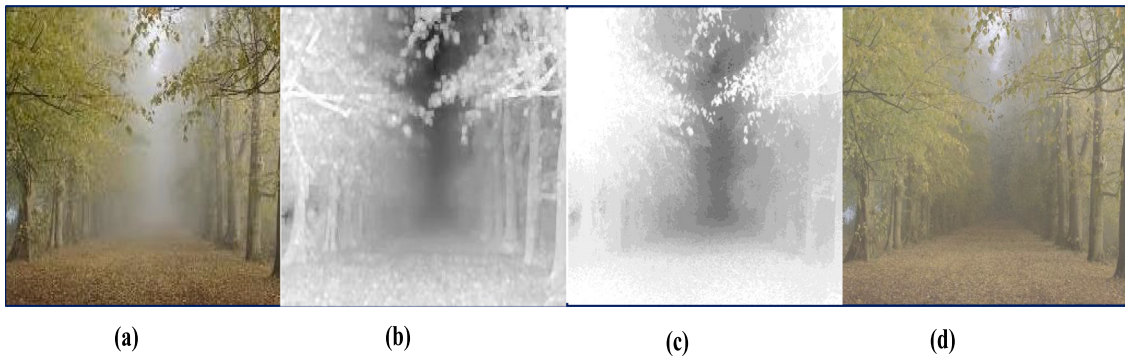


**Fig. 5.** (a) Hazy image (b) Transmission map [4] (c) Refined transmission map [4] (d) Dehazed output.

atmospheric light. The subsections below provided a detailed analysis of the proposed method.

### 3.1. Atmospheric light estimation

In general, atmospheric light is regarded as a light present in the majority of haze-opaque regions. In several single-image deweathering techniques preceding [4],  $A_l(x, y)$  is the highest pixel value in the dark channel. The method's analysis is based on the distance differentiation in the original images. The estimation of this term is a critical parameter, and even minor changes can have serious consequences as shown in Fig. 4. The selected patches in Fig. 4(a) represent the image's densest haze. The proper selection of pixels intensity values yields correct results as shown in Figs. 4(b) and 4(c). The He et al. [4] method's restored output was unsuccessful in eradicating the haze from the images in Fig. 4(b). The proposed method yields a significant and acceptable dehazed output, as indicated by the red box in Fig. 4(c). Recent techniques encourage the use of choosing the appropriate pixel intensities to represent atmospheric light  $A_l(x, y)$ . The image segmentation method introduces a new dimension to the estimation of atmospheric light  $A_l(x, y)$ .

- Steps:**
- (1) Initial assessment of  $T_{hre}$
- (2) Segmentation with  $T_{hre}$

(a) A1 pixel greater than  $T_{hre}$

(b) A2 pixels darker than  $T_{hre}$  or equal to  $T_{hre}$

(3) Using these steps as a basis, Eq. (1) can be modified as follows:

$$\frac{I_i^c(x, y)}{A_i^c(x, y)} = t(x, y) \frac{J_{ri}^c(x, y)}{A_i^c(x, y)} + 1 - t(x, y) \quad (13)$$

Assuming  $d_{sd}(x, y) \rightarrow \infty$ , from Eq. (5),

$$I_i(x)^c(x, y)_{d_{sd}(x, y) \rightarrow \infty} = A_i^c(x, y) \quad (14)$$

In (14), atmospheric light  $A_i^c(x, y)$  is described as:

$$A_i^c(x, y) = \max(I_i^c(x, y)) \quad (15)$$

Most researchers made the assumption that  $d_{sd}(x, y) \rightarrow \infty$  was correct in order to estimate the  $A_i^c(x, y)$  accurately. These presumptions, however, are never fulfilled in order to achieve these conditions. The mathematical modeling based technique with  $A(x, y)$  provides a wider range of estimates in order to improve. The initial step is to identify the scene's minimal components that correspond to the specified color channel index. By selecting the appropriate threshold values, non-atmospheric light intensity can be excluded.

$$\tilde{A}_i^c(x, y) = \begin{cases} A_1(x, y), & A_1(x, y) \geq Thre \\ A_2(x, y) & \text{otherwise} \end{cases} \quad (16)$$

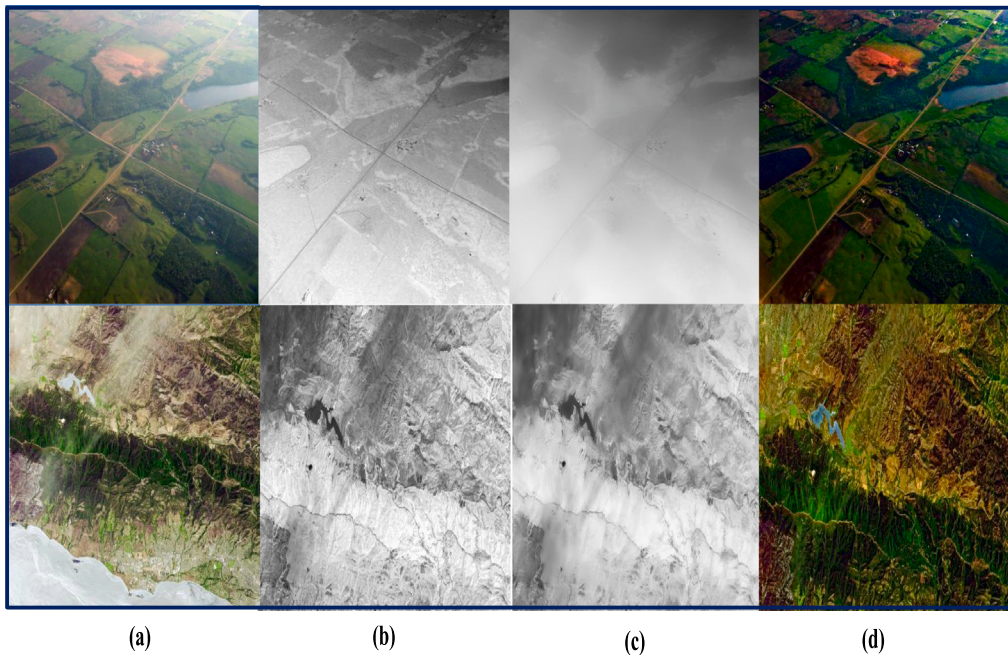


**Fig. 6.** (a) Different remote sensing hazy images (b) Transmission map (c) Refined transmission map (d) Dehazed output.

The symbol  $\tilde{A}_l^c(x, y)$ , which represents the scene's pixel intensity range, is used to find the maximum pixel intensity with threshold range.

$$A(x, y) = \max(\tilde{A}_l^c(x, y)) \quad (17)$$

The highest spread intensity in the high-intensity region should be taken into account to precisely estimate the atmospheric light  $A(x, y)$ .

### 3.2. Transmission map refinement

Satellite image quantity and quality have been significantly enhanced over the past few years as a result of tremendous advancements in remote sensing dehazing technologies. The sharpness of the image is significantly diminished in haze conditions because of the scattering of water vapor and dust particles in the air, making it challenging for many outdoor vision systems, such as those for object detection, object recognition, surveillance, and driver assistance, to perform further processing and operation. However, previous dehazing techniques frequently suffer from issues such as inadequate brightness, halos, artifacts, and blurring. The proposed solution is to compensate for the depth of variability in the transmission map in order to efficiently extract extensive analysis of the visibility of foggy images. In order to estimate the refined transmission map, the utilization of assumptions and constraints makes it easier to produce a solution. Eq. (3) demonstrates a simple method for calculating the transmission map, which can then be used to solve Eq. (1) for the three color channels on both sides, as shown below:

$$\min_{y \in \Omega(x)} (\min_{ce(r,g,b)} (\frac{I^c(y)}{A^c})) = \tilde{t}(x, y) \min_{y \in \Omega(x)} (\min_{ce(r,g,b)} (\frac{J^c(x)}{A^c})) + 1 - \tilde{t}(x) \quad (18)$$

$J$  dark channel is near to zero because it is a haze-free image. Eq. (4) refers to it as follows:

$$J^{dark}(x) = \min_{y \in \Omega(x)} (\min_{ce(r,g,b)} (J^c(y))) = 0 \quad (19)$$

This supposition enables us to comprehend the variable  $\tilde{t}(x, y)$  in Eq. (18) as a initial calculation of the transmission map. Regardless of the fact that there is limited modification and that it is detailed, the edges are difficult to discern. The refined transmission map employs the soft matting approach to get removal of the halo artifacts that were present at the edges of the initial transmission map [4]. Unfortunately,

there are still halos artifacts towards the boundaries of the refined transmission map image as shown in Fig. 5. Based on the initial transmission map  $\tilde{t}(x, y)$ , propose a solution to refine the transmission map in order to resolve this problem. The unsharp mask-based guided filtering method has been applied to achieve the best possible results in haze and fog removal. Fig. 6(a) depicts different remote sensing hazy images. The transmission map with an uneven distribution implies variations is shown in Fig. 6(b). Fig. 6(c) illustrates all the different remote sensing images that were employed to verify the significance of refining the transmission map in order to retrieve the final output. The restored dehazed output is shown in Fig. 6(d) by using presented method. The proposed approach is defined as follows:

$$T_{est}(x, y) = c \cdot \left( 1 - w \min_c \left( \min_{(y) \in \Omega(x)} \left( \frac{I^c(y)}{A^c} \right) \right) \right) \quad (20)$$

where,  $T_{est}(x, y)$  is initial transmission map. The refined transmission map  $T_{ref}(x, y)$  can be obtained as:

$$\hat{T}_{ref(i)}(x, y) = \frac{1}{|w|} \sum_{k \in w_i} (a_k G_i + b_k) \quad (21)$$

where refine transmission map is represented by  $T_{ref}(x, y)$ , an initial transmission map by an unsharp mask by  $(T_{est}(x, y) - f_L T_{est}(x, y))$  where  $f_L$  denotes a low-pass filter. By structurally transferring from a different guidance image, the edge enhancement task is carried out by directed filtering similarly to unsharp masking.

$$\hat{T}_{ref}(x, y) = \frac{1}{|w|} \sum_{k \in w_i} (a_k G_i + b_k) \quad (22)$$

In a manner similar to unsharp masking, we wish to keep only the coefficient in order to regulate the amount of structure:

$$\hat{T}_{ref(i)}(x, y) = \frac{1}{|w|} \sum_{k \in w_i} a_k G_i + \frac{1}{|w|} \sum_{k \in w_i} \bar{I}_k - a_k \bar{G}_k \quad (23)$$

$$\hat{T}_{ref(i)}(x, y) = \frac{1}{|w|} \sum_{k \in w_i} a_k (G_i - \bar{G}_k) + \hat{T}_{est(i)}(x, y) \quad (24)$$

where,

$$\hat{T}_{est(i)}(x, y) = \frac{1}{|w|} \sum_{k \in w_i} \bar{I}_k \quad (25)$$

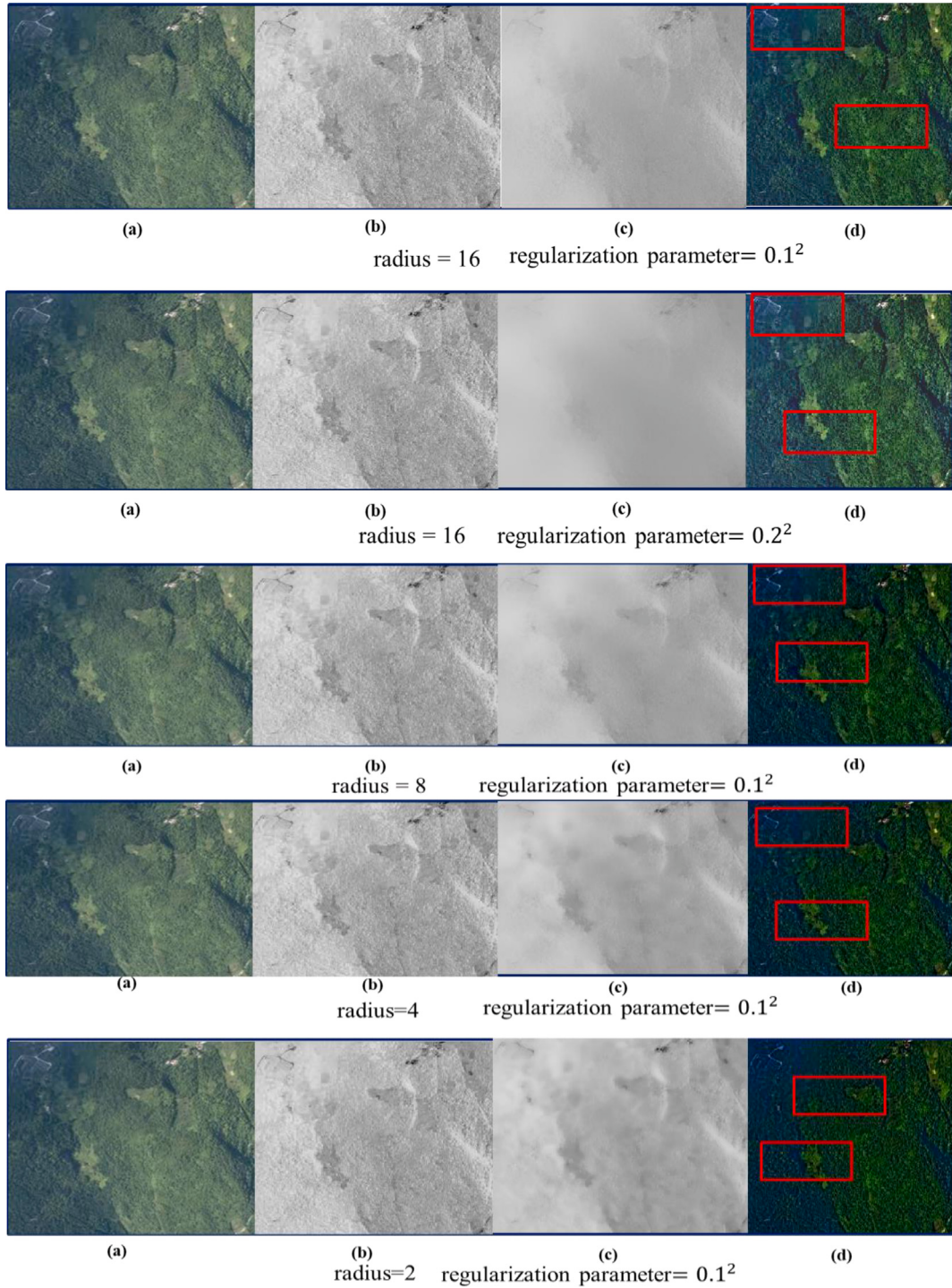


Fig. 7. (a) Original image. (b) Transmission map (c) Refine transmission map (d) Dehazy images.

The guiding image should be in grayscale or a single-channel image with a local window radius of 2, 4, 6, 8, or 16. However, the window radius for detailed enhancement was set to 16, although it may change depending on the usefulness of various image-smoothing scenarios. The regularization parameter was set to  $0.1^2$ . It may vary depending on the manner in which the images are smoothed for transmission-depth estimation as shown in Fig. 7.

$$T_{ref(i)}^\wedge(x, y) = \bar{a}_i(G_i - \bar{G}_i) + T_{est(i)}^\wedge(x, y) \quad (26)$$

The formula in Eq. (28) assists us to determine how the guided filter inherently accomplishes edge-preservation and model-transferring. The coarse transmission map  $T_{est}(x, y)$  is specifically smoothed to remove extraneous elements and outcome is shown by  $\tilde{T}_{est(i)}(x, y)$ . The lack of sharp edges during the smoothing process, however, produces output which appears blurry. An unsharp mask  $(G_i - \bar{G}_i)$  with fine edges produced from the  $G$  is applied to  $\tilde{T}_{est(i)}(x, y)$  under the coefficient  $a$ , as a result, the guide image's structure is carried through to the filtered output image  $T_{ref(i)}^\wedge(x, y)$ .

### 3.3. Estimating the scene radiance

Once the atmospheric light and the transmission map have been analyzed, Eq. (18) can be solved to calculate the radiation of the scene:

$$J^c(x, y) = \frac{I^c(x, y) - A^c(x, y)}{\max(\hat{T}_{ref}, t_o)} + A^c(x, y) \quad (27)$$

The noise in the scene arises from the instantaneous restoration of the radiance  $J^c(x, y)$ . The transmission  $\hat{T}_{ref}$  must be limited to a lower limitation of  $t_o$  (typically 0.1) in order to retain some fog. Algorithm 1 outlines the complete process of estimating  $J^c(x, y)$  to ensure clarity.

---

**Algorithm 1: The Proposed Deweathering Algorithm**


---

**Input:** Hazy and Foggy Image  $I(x, y)$

**Do the Job:**

1. Calculate the minimum pixel intensities for each color channel.
2. To accurately approximate pixel intensity, set the threshold range.
3. Find the highest intensity possible within the given parameters.
4. Consider the ambient light for the original image to be the region of highest intensity with the greatest spread of intensity.
5. Estimate coarse transmission map ( $T_{est}(x, y)$ )
6. smoothed to remove undesirable elements like noise and textures, as indicated by  $\tilde{T}_{est(i)}(x, y)$
7. unsharp mask ( $G_i - \tilde{G}_i$ ) is used for refine transmission map  $\hat{T}_{ref(i)}(x, y)$

---

**8. Output:** Image recovery without haze  $J^c(x, y)$

---

## 4. Performance metrics

This section compares the results with state-of-the-art techniques using performance metrics such as PSNR (Peak Signal-to-Noise Ratio), MSE (Mean Squared Error), SSIM (Structural Similarity Index), UQI (universal image quality index), FADE (fog aware density evaluator) [62], DHQI (dehazing quality index) [63], Standard deviation (CC) [69] and Blind contrast enhancement assessment ( $e$  and  $r$ ) [70].

### 4.1. Mean Squared Error (MSE)

It calculates the error similarity between the restored image and the original image, which is determined as follows:

$$MSE(X, Y) = \frac{1}{R \cdot S} \sum_{X=1}^R \sum_{Y=1}^S (M(X, Y) - N(X, Y))^2 \quad (28)$$

where  $M(X, Y)$  and  $N(X, Y)$  are the foggy image and the restored image, respectively. The image's length and width are  $R$  and  $S$ .

### 4.2. Peak Signal-to-Noise Ratio (PSNR)

It calculates spatial reconstruction quality between the original and restored images, which is defined as,

$$PSNR(X, Y) = 10 \log_{10} \frac{A^2 R \cdot S}{\sum_{X=1}^R \sum_{Y=1}^S (M(X, Y) - N(X, Y))^2} \quad (29)$$

$$= 10 \log_{10} \frac{A^2}{MSE} \quad (30)$$

where  $A$  is the image gray level.

### 4.3. Structural Similarity Index (SSIM)

It determines the structural similarities between the referred and restored data, which are calculated as,

$$SSIM(X, Y) = \frac{1}{N} \sum_{i=1}^N \frac{(2\mu_{X_i}\mu_{Y_i} + c_1)(2\sigma_{X_i}Y_i + c_2)}{(\mu_{X_i}^2 + \mu_{Y_i}^2 + c_1) + (\sigma_{X_i}^2 + \sigma_{Y_i}^2 + c_2)} \quad (31)$$

### 4.4. Universal image quality index (UQI)

It refers to the similarity between the restored and referenced data in terms of brightness, contrast, and structure, which is described as,

$$UQI(X, Y) = \frac{1}{N} \sum_{i=1}^N \frac{4\sigma_{X_i}Y_i\mu_{X_i}\mu_{Y_i}}{(\sigma_{X_i}^2 + \sigma_{Y_i}^2)(\mu_{X_i}^2 + \mu_{Y_i}^2)} \quad (32)$$

where  $\sigma_{X_i}Y_i$  is the covariance of  $X_i$ , and  $Y_i$  and  $\mu_{X_i}$  and  $\mu_{Y_i}$  are the mean values of  $X_i$ , and  $Y_i$ , respectively.

### 4.5. FADE and DHQI

FADE is a framework for predicting non-reference visual fog densities based on statistical features that account for fog along with information from the actual image. Lower FADE values for dehazing indicate better performance, implying less fog and haze in the final output. In contrast to FADE, a higher DHQI demonstrates better performance in retrieving output.

### 4.6. Standard deviation (CC)

The standard deviation (the square root of variance) was employed to measure image contrast in the literature [69]. As stated in [71], the standard deviation (patch  $p$ ) used to determine the local color contrast of a haze-free image is as follows:

$$CC_p = \sqrt{\frac{1}{N_k - 1} \sum_{k=1}^{N_k} (\bar{J}_{pk} - J_p)^2} \quad (33)$$

$$\bar{J}_{pk} = \frac{1}{N_{pk}} \sum_{x \in \varphi_{pk}} J(x) \quad (34)$$

$$J_p = \frac{1}{N_k} \sum_{k=1}^{N_k} \bar{J}_{pk} \quad (35)$$

Where,  $k$  is the index of color cluster,  $p$  is the index of image patch,  $J(x)$  is the color value of haze-free image in coordinates  $x$ ,  $\varphi_{pk}$  is a set of pixels which belong to the  $k$ th color cluster in patch  $p$ ,  $N_{pk}$  is the number of pixels in  $\varphi_{pk}$ ,  $\bar{J}_{pk}$  is the mean value of pixels in  $\varphi_{pk}$ ,  $N_k$  is the number of clusters in patch  $p$ ,  $J_p$  is the mean value of  $\bar{J}_{pk}$ . Finally, the mean value of  $CC_p$  to measure the overall Color Contrast (CC) of the entire haze-free image is:

$$CC = \frac{\frac{1}{N_p} \sum_{p=1}^{N_p} CC_p}{\sqrt{\frac{1}{H \cdot W - 1} \sum_{i=1}^H \sum_{j=1}^W (I_{(i,j)} - \bar{I})^2}} \quad (36)$$

Where,  $N_p$  is the number of patches in the whole haze-free image.  $[H, W]$  denote the dimensions of the image.  $I_{(i,j)}$  is the color value of the hazy image in coordinates  $(i, j)$ .  $\bar{I}$  is the mean color of the hazy image  $I$ .

### 4.7. Blind contrast enhancement assessment ( $e$ and $r$ )

To assess the effectiveness of each restoration procedure, we have incorporated more well-known quantitative indicators such  $e$  and  $r$  [70]. After restoration, the indicator  $e$  symbolizes edges that are now clearly visible. It is stated as:

$$e = \frac{n_r - n_o}{n_o} \quad (37)$$

where,  $n_r$  and  $n_o$  are the number of visible edges in the original image and the restored image. The other parameter is the  $r$ , which is the average gradient ratio before and after restoring foggy images.

$$r = \frac{g_r}{g_o} \quad (38)$$

Where,  $g_r$  and  $g_o$  are the average gradients of the original image and the restored image. Higher  $e$  and  $r$  values for haze diminution result in better restoration effects.

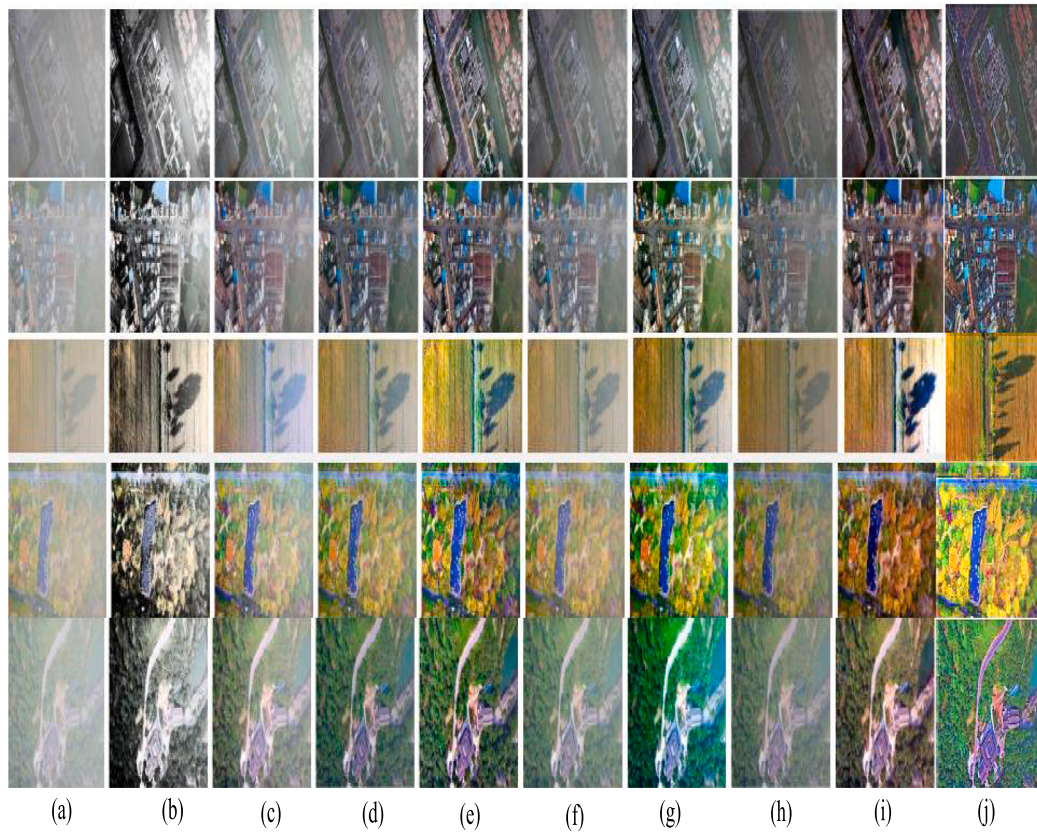


**Fig. 8.** (a) Original image. (b) He et al. method [4] (c) Retinex [12] method (d) DCP [21] (e) Berman et al. [10] method (f) cai et al. [42] method (g) Ren et al. [43] method (h) Lie et al. [44] method (i) GCANet [45] method (j) Proposed method.

## 5. Comparison and experimental results

Several cutting-edge techniques have been compared to the proposed method to demonstrate its effectiveness, including those developed by Zhu et al. [27], Pan et al. [29], artificial multi-exposure image fusion (AMIF) [35], He et al. method [4], Fattal [5], Retinex [12], Berman et al. [10], IDeRS [33], Xie et al. [31], Shin et al. [47], Liu et al. [49], Kumar et al. [50], Shen et al. [59], Ju et al. [60], and Han et al. [61]. Furthermore, in order to illustrate the efficacy of the proposed technique, it was compared to a number of recent deep learning methods, such as Cai et al. [42], Ren et al. [43], Li et al. [44], Multilayer perceptron (MLP) [46], Mehta et al. [55], H. Li et al. [57], and Dong et al. [72] methods.

The SateHaze1k dataset [52] and AID [53] datasets, which contain synthetic RS (remote sensing) images with various amounts of haze as well as explicit homogeneous hazy image pairs, have been used to assess the performance of the present work. The numerous RS photos from the real world are also included to validate this research. Both quantitatively and qualitatively, the performance of the defogging outcomes of remote sensing photos was assessed. The original, clear image is used as the baseline for all quality indices calculations. An Intel (R) Core (TM) i5-8265U CPU running at 1.80 GHz and 8.00 GB of RAM were used to execute all algorithms in the MATLAB environment.

### 5.1. Qualitative comparison

Remote sensing images are significantly affected by hazy weather conditions. For the assessment to qualitatively analyze the effectiveness of the various approaches, several real-world remote sensing images were taken. These hazy image data, as depicted in Fig. 6, are collected from Google Earth for methodological experimentation. From the Remote sensing Image Cloud rEmoving dataset (RICE 1), further remote sensing images are also acquired [51].

The recovered output contrast is decreased and any objects present in those images are not discernible using the method by Zhu et al. [27]. Since the Pan et al. [29] method is unable to precisely estimate the transmission map, the resulting images still contain haze. The resulting images, which exhibit color distortion, are overly enhanced by the IDeRS [33] method. Using the AMIF [35] method, the restored output was not completely free of haze. The proposed method, in contrast, produces dehazing images that are noticeably clearer while maintaining the edges.

The additional sets of remote sensing images and commensurate deweathering images are shown in Fig. 8. The restored images by He et al. [4] and the Retinex method [12] have high contrast, but the color distortion is significant. Berman's method preserves the edges effectively, but it introduces artifacts. The use of the approaches [42, 43], and [44] to produce high-quality dehazed images may not completely eliminate halo effects.

The results of various approaches, including deep learning methods and the proposed approach, are shown in Figs. 9 and 10. The dehazing results obtained by He et al. [4] approach has a low contrast. The Ren et al. [43] approach fails mostly by training for synthetic hazy images despite having a better contrast than the He et al. [4] method. The enhanced version of He et al. approach in [29] is also unsuitable for removing haze and fog from hyperspectral images. The recovered output of the dark channel approach sometimes incorporates artifacts or introduces new components because it depends strongly on assumptions. The MLP [46] approach uses contrast stretching to improve brightness and produce halos in the resulting images. Contrast stretching produces equivalent outcomes, however one's selection of the settings affects this. Compared to previous methods, IDeR's method [33] produces dehazed output that is more robust but also more distorted in terms of color. Due to the inadequacy of the dark channel-saturation prior to create a correlation between the dark channel and saturation of haze-free images, the ADM approach for removing fog from hyperspectral

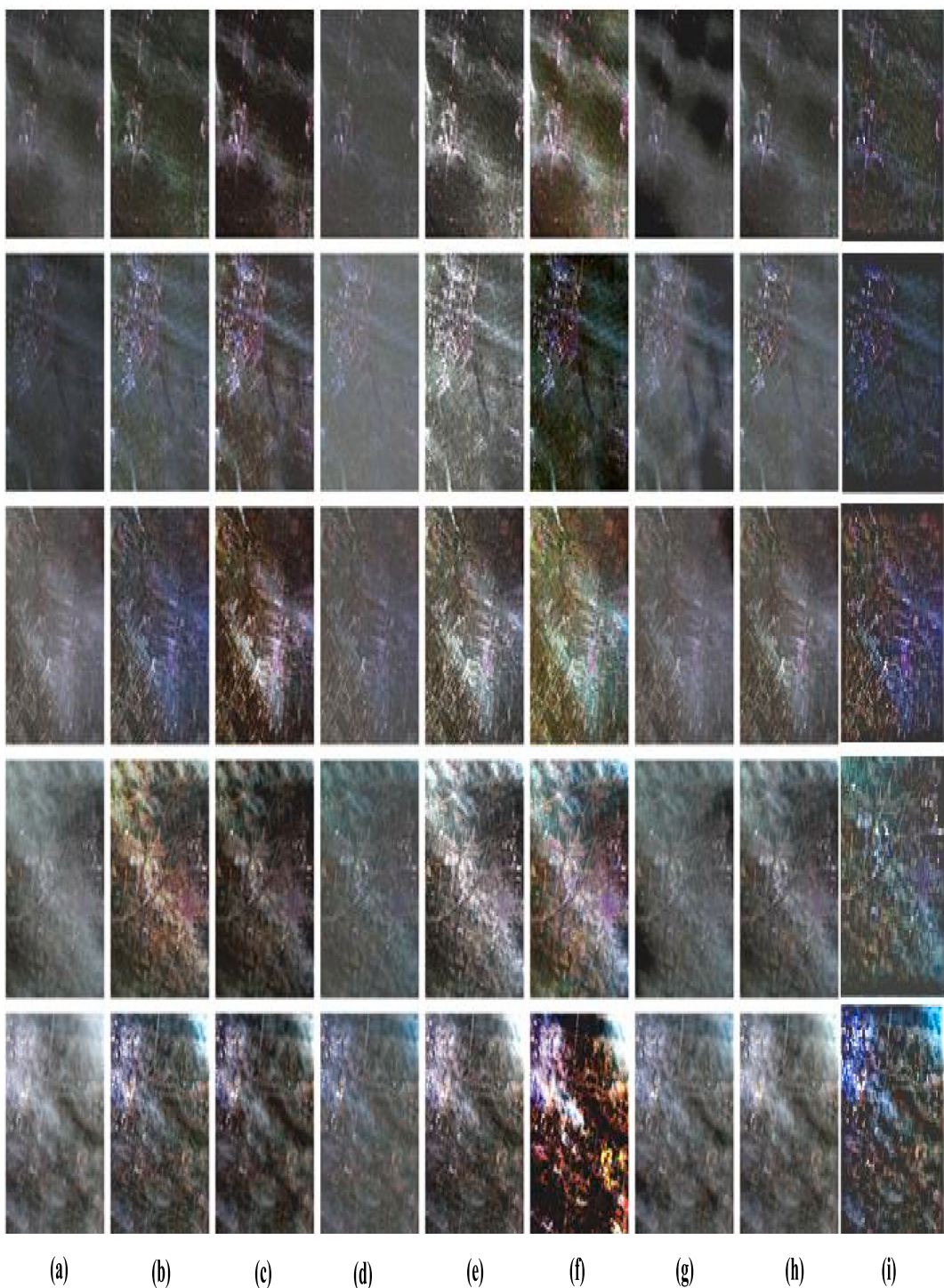


**Fig. 9.** (a) Original image. (b) He et al. [4] (c) Ren et al. [43] (d) Pan et al. [29] (e) MLP [46] (f) IDeRS [33] (g) Xie et al. [31] (h) Shin et al. [47] (i) Proposed method.

images fails. Images recovered using the Shin et al. [47] approach still contain fog.

Fig. 11 shows that the dehazing results obtained by He et al. [4] and Fattal [5] were not satisfactory and that some residual haze had a blurring impact. Although Berman's approach improved visibility, it also increased light exposure in some areas. The output has been restored, and it seems evident that more green has been added. The Liu et al. method [49] used a contrast enhancement method to boost the brightness, although color distortion was found in the reconstructed image. The output reconstructed by Kumar et al. [50] performed better,

however, color variation was noticeable. The proposed approach efficiently restores deweathering images while maintaining color accuracy. Furthermore, the approach retrieves more distinct details.

For a fair visual comparison on the StaeHaze 1kDatasets, different types of synthetic remote sensing images were used, including ground truth (GT) images. The various dehazing procedures can only remove haze to a limited amount and are not ideal for thick hazy conditions as shown in Figs. 12 and 13. Figs. 12(a) and 13(a) depict the thick hazy images. The red square box in Figs. 12(b) and 13(b) indicate that the Cai et al. [42] presented approach still consist of haze. Figs. 12(c)–(d) and 13(c)–(d) recovered the images and were similar to GT, however

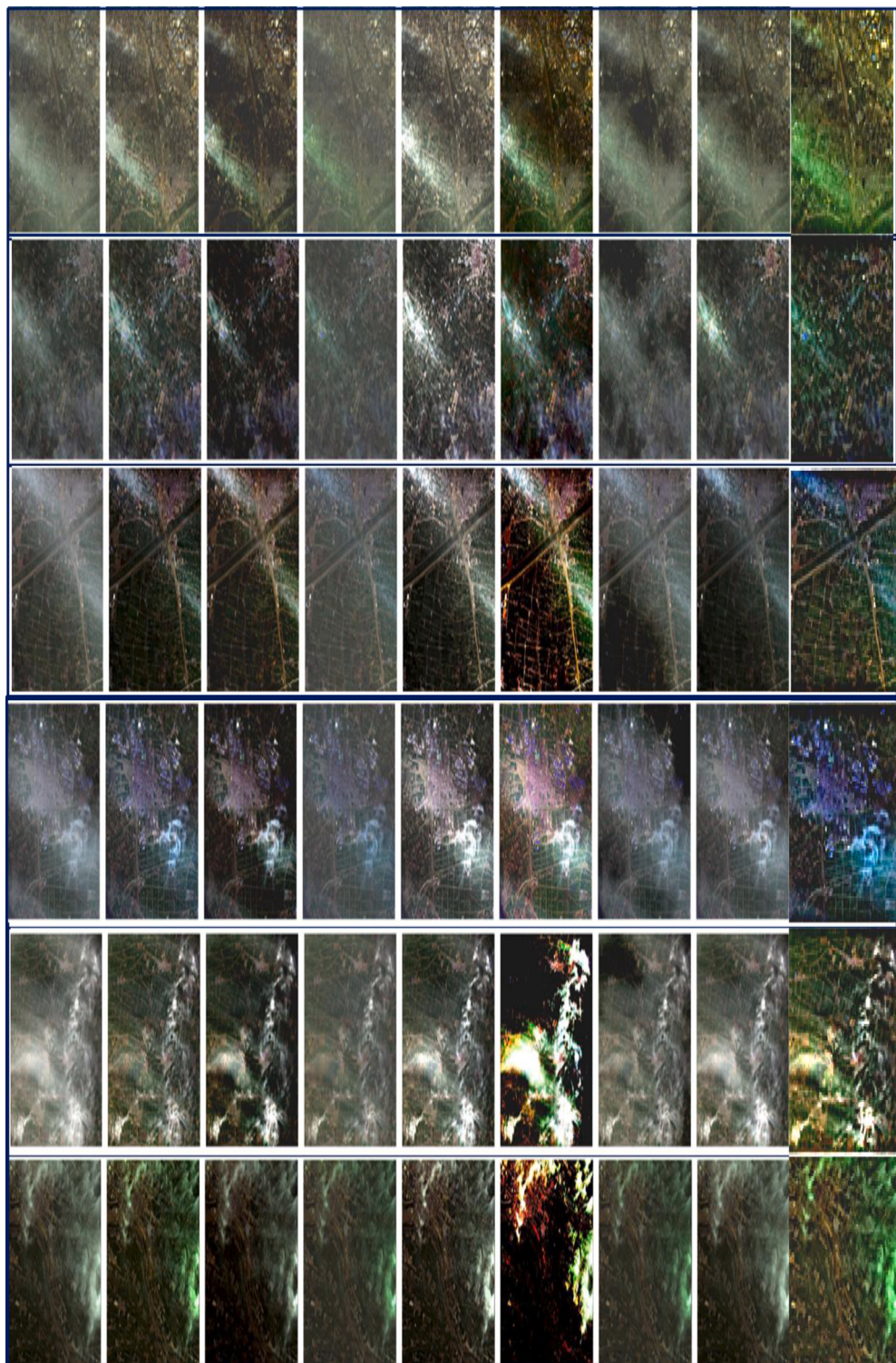


**Fig. 10.** (a) Original image. (b) He et al. [4] (c) Ren et al. [43] (d) Pan et al. [29] (e) MLP [46] (f) IDeRS [33] (g) Xie et al. [31] (h) Shin et al. [47] (i) Proposed method.

color differences were shown. In Figs. 12(e) and 13(e), there is higher contrast, which results in more saturated pixels. It has been noticed that the haze was not completely eradicated in Figs. 12(f)–(g) and 13(f)–(g). The proposed methodology preserves contrast and can handle most hazy scenarios ranging from thin to dense haze.

In general, as demonstrated in Figs. 14 and 15, the haze imparted more brightness and whiteness than the restored images. Figs. 14 and 15 provide illustrations of the recovered outputs using various state-of-the-art techniques. The recovered results in Figs. 14(b), (e), (f), and

15(b), (e), (f) still contain remnant haze, which are indicated by the blue and red square boxes. In comparison to [42,54], and [60], the results from other dehazing procedures are statistically satisfactory. These methods, however, have artifacts around trees and areas for parking. The method that is being discussed preserves the edges while avoiding excessive brightness.

Fig. 16 depicts two image sets (House and Pumpkin) that represent various widely employed hazy images and the corresponding results of dehazing techniques. The outcomes of alternative dehazing techniques

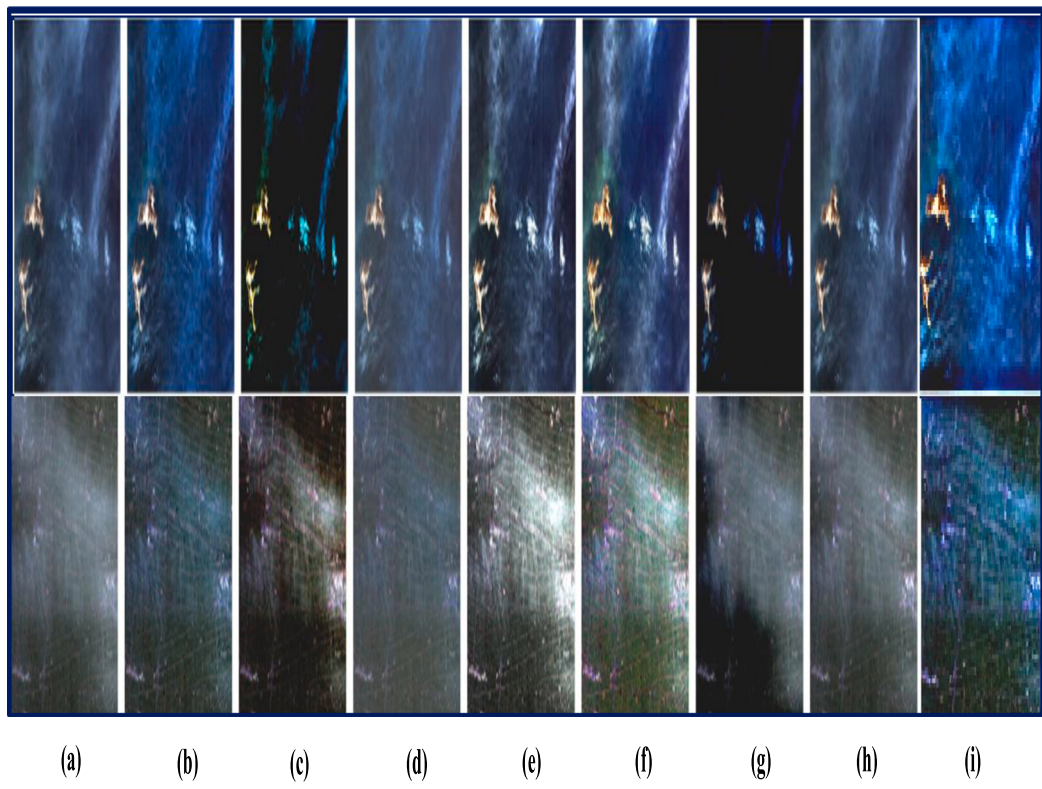


Fig. 10. (continued).

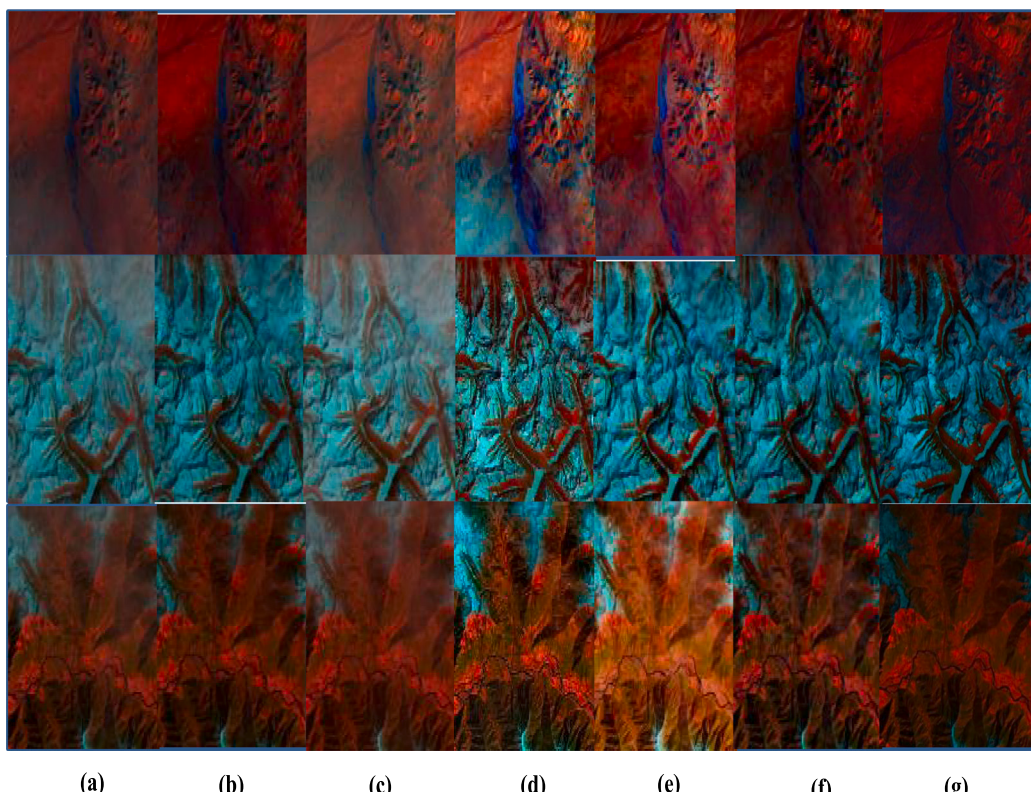
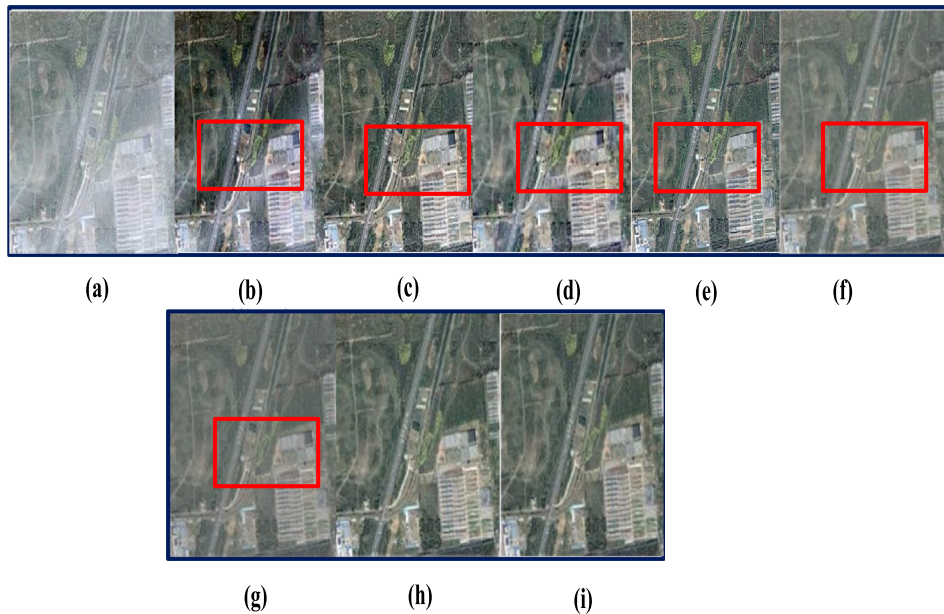
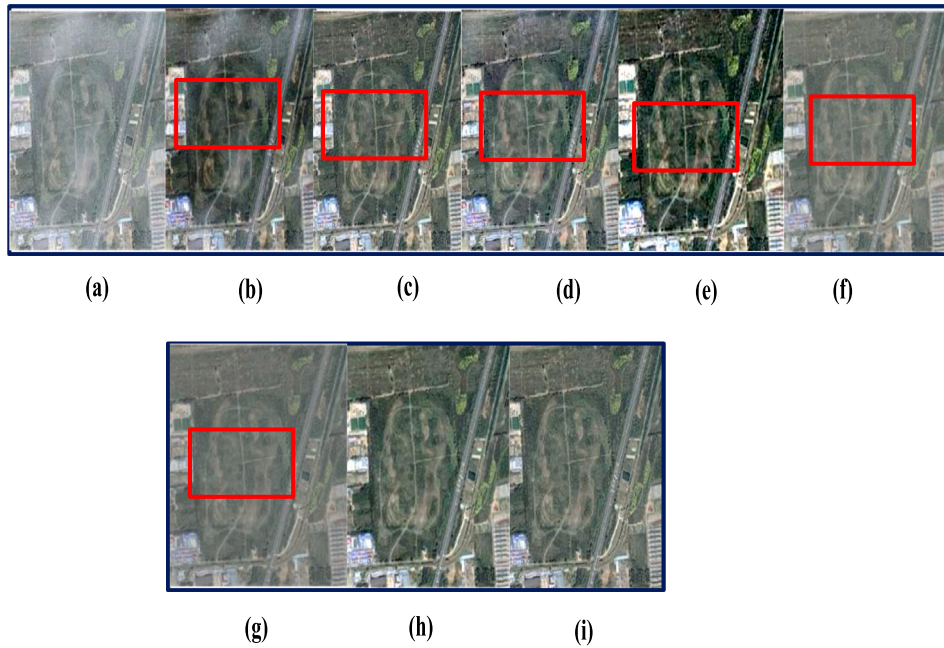


Fig. 11. (a) Original image. (b) He et al. [4] (c) Fattal [5] (d) Berman et al. [10] (e) Liu et al. [49] (f) Kumar et al. [50] (g) Proposed method.



**Fig. 12.** (a) Original image. (b) cai et al. [42] (c) Huang et al. [52] (d) Mehta et al. [55] (e) Bie et al. [54] (f) H. Li et al. [57] (g) Dong et al. [72] (h) Proposed method (i) GT.



**Fig. 13.** (a) Original image. (b) cai et al. [42] (c) Huang et al. [52] (d) Mehta et al. [55] (e) Bie et al. [54] (f) H. Li et al. [57] (g) Dong et al. [72] (h) Proposed method (i) GT.

are statistically acceptable compared with those of [4,5], and [10]. The approach being explored retains the edges while maintaining the perceptual quality.

### 5.2. Quantitative comparison

Nine commonly used objective metrics, including the MSE, SSIM, PSNR, UQI, FADE, DHQI, CC,  $e$ , and  $r$  are adopted in order to evaluate quantitatively the defogging performance of various approaches.

The restoration quality of various dehazing approaches is evaluated in **Table 1** by comparing a series of remote sensing images assessments in terms of MSE and PSNR metrics. The dehazing performance of the proposed methodology is further substantiated by the fact that it

persistently performs all other approaches in terms of SSIM, and UQI. In the Lie et al. [44] approach, the PSNR values are higher for Images 1, 3, and 4. In comparison to other methods described, Cai et al. [42] methodology for Image 5 has greater PSNR values. A higher PSNR value indicates improved dehazing performance. Lower values for the MSE index indicate less severe visual distortion. The table concludes that the proposed method has the significant PSNR values among all approaches.

**Table 2** quantitative results demonstrate that our approach can consistently outperform conventional defogging techniques among all criteria, which is commensurate with the outcomes that can be seen. The proposed approach improves the following metrics over the existing comparison methods: SSIM from 0.6762 to 0.9747, PSNR from

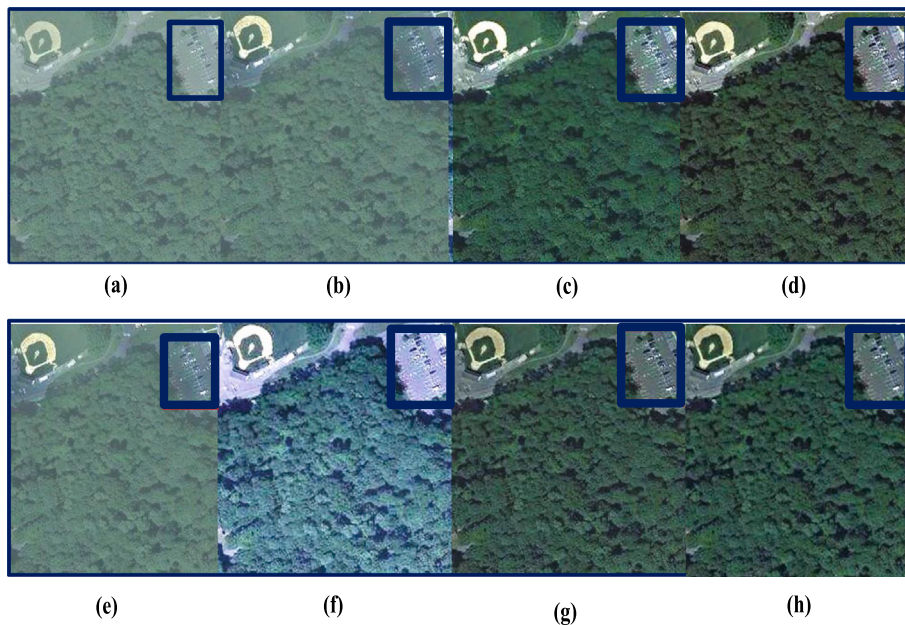


Fig. 14. (a) Original image. (b) Xie et al. [31] (c) Xu et al. [33] (d) Berman et al. [10] (e) Shen et al. [59] (f) Ju et al. [60] (g) Han et al. [61] (h) Proposed method.

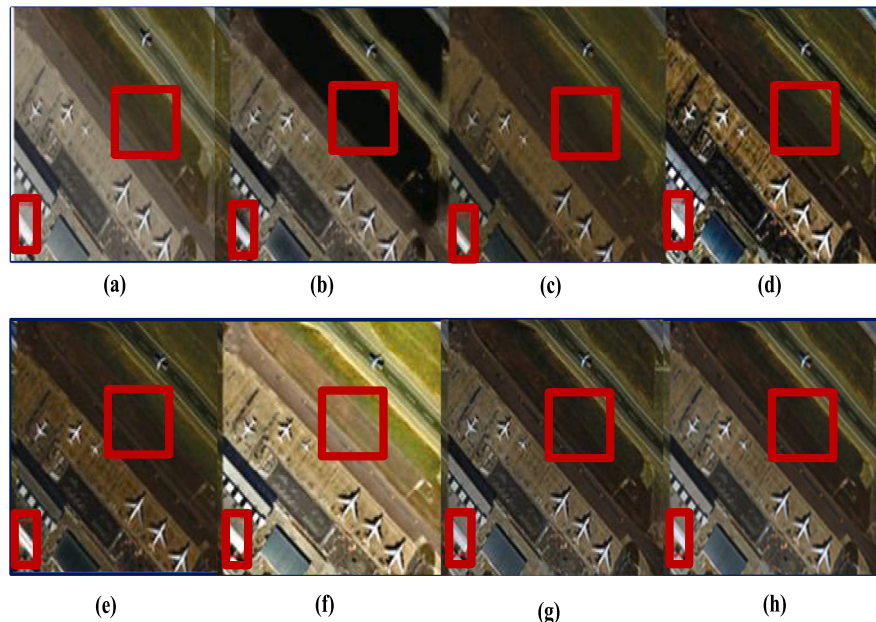


Fig. 15. (a) Original image. (b) Xie et al. [31] (c) Xu et al. [33] (d) Berman et al. [10] (e) Shen et al. [59] (f) Ju et al. [60] (g) Han et al. [61] (h) Proposed method.

14.6295 to 29.4153, and UQI from 0.6255 to 0.9306 for Figs. 6 and 7. These outcomes demonstrate that the presented methodology can more effectively preserve and restore high-quality images. The SSIM, PSNR, and UQI illustrate more effective or equivalent results to the existing recent approaches for Fig. 8. The proposed approach works more effectively and maintains color without diminishing details.

Table 3 compared the results of the proposed methodology to the techniques employed by Cai et al. [42], Huang et al. [52], Mehta et al. [55], and Bie et al. [54] in order to assess its efficacy on synthetic StaeHaze 1kDatasets. The proposed technique exhibits greater values in Table 3 when compared to various hazy conditions. The use of this method restores the dehazy remote sensing images and works efficiently for thin to thick haze, especially in more hazy situations.

The two image quality metrics employed for a quantitative assessment of various dehazing techniques are summarized in Table 4. The

scores obtained for the proposed technique are comparable to [10,61], and it achieves satisfactory scores when compared to other dehazing methods.

Table 5 shows that Gibson and our technique perform better on contrast enhancement in house images than He et al. [4] and Berman et al. [10] according to the values of CC. The outcomes of the proposed method for improving visibility are equivalent to or superior according to the values of  $e$  and  $r$ . Gibson et al. [73], Fattal [5], and Berman et al. [10], all of which outperformed dehazing in the case of a pumpkin image in terms of contrast enhancement. The values of  $e$  and  $r$  show that the proposed method and Gibson et al.'s [73] work produced the best results for visible-edge enhancement.

The most significant advantage of the presented approach is its reduced computing complexity in addition to its enhanced perceptual

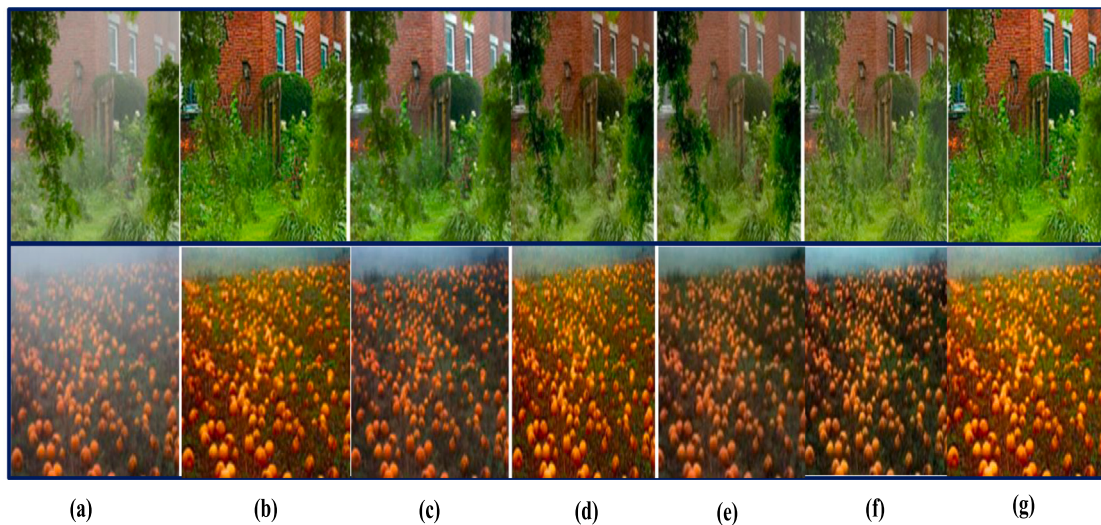


Fig. 16. (a) Original image. (b) Gibson et al. [73] (c) song et al. [71] (d) Fattal [5] (e) He et al. [4] (f) Berman et al. [10] (g) Proposed method.

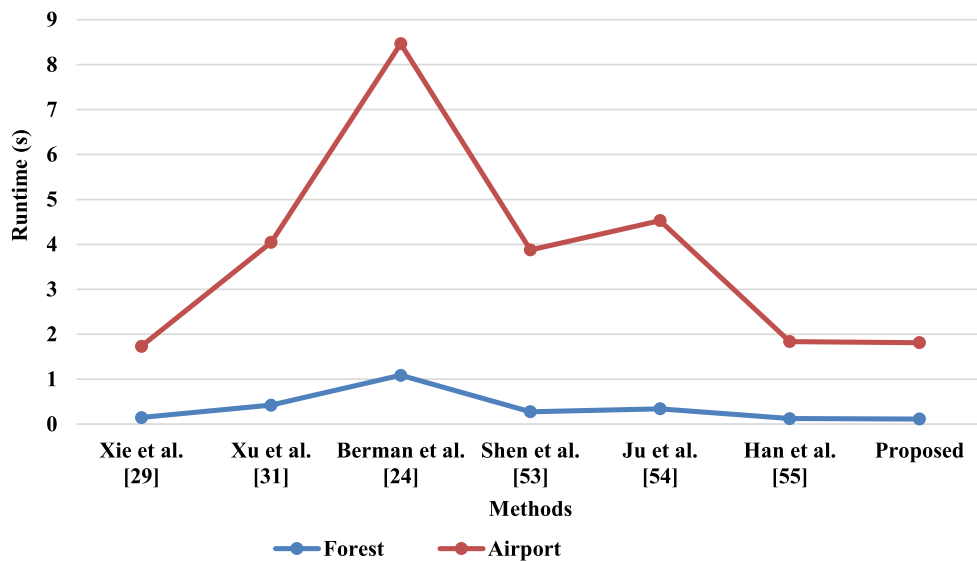


Fig. 17. Comparison of run-times for various dehazing methods.

quality. To ensure appropriate results and fair comparison, all approaches were implemented in MATLAB. The computing complexity is comparable to or even high in [33] since it primarily depends on the virtual depth and iterative procedure for estimate of the depth for dehazing. Other approaches, such as Berman et al. [10] and Shen et al. [59], rely substantially on assumptions and spectral adaptation of the parameters to estimate transmission depth. In comparison to [31, 61], this work's overall execution time is nearly comparable or even faster as shown in Fig. 17.

## 6. Discussion

Low visibility can be exacerbated by atmospheric conditions such as haze and fog, which lower the contrast and color in remote sensing images. Consequently, in these situations, dehazing and defogging are vital for producing images with acceptable perceptual quality. The impressive outcome of eliminating haze and fog from remote sensing images leveraging the enhancement and restoration approach is simple, despite its features of halos and artifacts. Physical model-based strategies for dehazing have gained prominence, incorporating multiple stages of estimation for recovering the scene radiance. As a result,

comprehension regarding estimation at each stage is crucial; otherwise, color oversaturation prevails.

Based on [4], the obtained transmission map is accountable for the accuracy of the transmission map estimation in Eq. (6). As a result, inspired by enhancement-based methods of smoothing the transmission map; and finally, scene restoration, as demonstrated in Fig. 3. Equations (13)–(26), which are extensively explained in Section 3.1 and Section 3.2, can be employed to produce significant depth information and a precise haze distribution from a transmission map. The estimation of the transmission map is positively impacted by the correct selection of pixel intensity values, which estimates the atmospheric light and compensates for color distortions. The selection of proper pixel intensities to imitate atmospheric light is encouraged by modern approaches.

The physical based construct in [24,29] demonstrate the promising performance results by concatenating and collaboratively adjusting the transmission map. Although the produced images retain a haze or overly enhanced similar to other relevant works [33,34]. The recommended approach effectively recovers deweathered images while preserving color fidelity. The method also retrieves more precise information. Several dehazing techniques have been described [42–48,54, 55,59] on another set of synthetic annotated images, but all of them

**Table 1**  
Different dehazing approaches quantitative comparison results.

Image	Methods	Metric	
		MSE	PSNR
Im_1	He et al. [4]	63.8380	10.017
	Retinex [12]	74.9954	15.023
	DCP [21]	58.0916	17.284
	Berman et al. [10]	70.6542	12.516
	Cai et al. [42]	78.5197	15.348
	Ren et al. [43]	50.8604	16.926
	Lie et al. [44]	54.8527	18.178
	GCAINet [45]	61.5088	14.583
	Proposed method	44.3575	31.6951
	He et al. [4]	66.5203	9.9918
Im_2	Retinex [12]	84.4062	12.0322
	DCP [21]	50.1036	19.2096
	Berman et al. [10]	78.2738	13.7839
	cai et al. [42]	68.5316	16.9787
	Ren et al. [43]	57.0354	17.3780
	Lie et al. [44]	57.3905	17.9371
	GCAINet [45]	79.1826	13.0886
	Proposed method	43.8746	31.7427
	He et al. [4]	66.4734	8.2387
	Retinex [12]	78.6077	10.8556
Im_3	DCP [21]	74.9392	14.9927
	Berman et al. [10]	76.3182	10.4802
	cai et al. [42]	84.3603	12.7805
	Ren et al. [43]	60.7811	16.1591
	Lie et al. [44]	58.9837	17.7510
	GCAINet [45]	65.4599	12.0327
	Proposed method	46.1575	31.5224
	He et al. [4]	64.6617	8.6274
	Retinex [12]	79.2677	14.0277
	DCP [21]	71.7706	14.9921
Im_4	Berman et al. [10]	68.9340	13.4883
	cai et al. [42]	73.9023	15.6290
	Ren et al. [43]	50.3411	15.9782
	Lie et al. [44]	58.6004	17.6301
	GCAINet [45]	60.0329	14.5927
	Proposed method	50.5062	31.1314
	He et al. [4]	64.6617	12.1672
	Retinex [12]	79.2677	19.9542
	DCP [21]	71.7706	17.5611
	Berman et al. [10]	68.9340	21.0496
Im_5	cai et al. [42]	73.9023	22.7793
	Ren et al. [43]	50.3411	15.2877
	Lie et al. [44]	58.6004	20.5717
	GCAINet [45]	60.0329	21.1517
	Proposed method	43.2841	31.8015

**Table 2**  
PSNR, SSIM, and UQI comparison results.

Images	Methods	Metrics		
		SSIM	PSNR	UQI
Figs. 8 and 9	He et al. [4]	0.6762	14.6295	0.6255
	Ren et al. [43]	0.9085	25.8365	0.8797
	Pan et al. [29]	0.8558	21.9121	0.8264
	MLP [46]	0.7205	16.2691	0.6949
	IDeRS [33]	0.6133	14.1409	0.5959
	Xie et al. [31]	0.9039	23.2267	0.8724
	Shin et al. [47]	0.8019	17.9528	0.7731
	Proposed method	0.9747	29.4153	0.9306
	He et al. [4]	0.8330	20.7801	0.8949
	Fattal [5]	0.8366	22.101	0.9010
Fig. 10	Berman et al. [10]	0.6868	21.02	0.8411
	Liu et al. [49]	0.7534	22.5101	0.9158
	Kumar et al. [50]	0.7688	22.9100	0.8729
	Proposed method	0.8578	24.6039	0.9146

are not the best for thick hazy images. The StaeHaze 1k datasets were utilized to create a fair visual comparison using a variety of synthetic

**Table 3**  
Comparison of PSNR AND SSIM with state-of-the-art methods on SateHaze 1kDatasets.

Method	Thin Haze		Moderate Haze		Thick Haze	
	PSNR	SSIM	PSNR	SSIM	PSNR	SSIM
Cai et al. [42]	19.75	0.8950	18.12	0.8552	14.33	0.7064
Huang et al. [52]	24.16	0.9061	25.31	0.9264	25.07	0.8640
Mehta et al. [55]	25.38	0.9248	25.58	0.9035	23.43	0.8925
Bie et al. [54]	26.68	0.9245	26.02	0.9294	26.71	0.9285
Proposed	35.10	0.9356	34.81	0.9319	35.17	0.9389

remote sensing images, including ground truth (GT) images like the ones shown in Fig. 12.

Deep learning techniques are continually developing, and the utility of convolution neural network (CNN) approaches in a wide range of applications such as segmentation and picture dehazing has been established [37–41]. To dehaze remote sensing images, deep learning techniques have recently been used with feature extraction [8,54–58]. These approaches produced statistically significant results. These techniques, however, rely more on feature analysis and require larger training datasets. Therefore, it is ineffective to directly convolute the original remote sensing images using a neural network for dehazing. For proper dehazing and defogging without color distortion, it is crucial to completely utilize the primary insights regarding the physics-based model and enhancement-based procedures. Therefore, the physical model incorporates the concept of threshold-based methods and Unsharp mask guided filtering to dehaze images while maintaining perceptual quality. Thus, compared with the latest methods, the proposed method provides better performance.

In comparison to the other techniques, the execution times were approximately identical and even faster. The solution offered successfully eliminates haze while maintaining the true nature of the scene. Figs. 8–13 show the results for all haze removal methods. The performance metric values for several datasets, including real-world remote-sensing images, were determined. In terms of all estimated metrics, it was observed that the recommended approach performed noticeably better than the others. As can be observed from the results presented, the performance of the proposed method for dehazing satellite imagery is robust and consistent. Finally, Tables 1–5 provide an outline of the main contributions of this study for enhancing the performance and computational effectiveness based on the experimental results for various datasets.

## 7. Application areas

Visibility restoration, which is fast and effective, is advantageous for a wide range of real-world applications. Exploration of the ecological environment, earth resources, and human activities can all be performed using remote sensing images. RS images are typically influenced by haze or fog when captured from a distance, which lowers their quality and limits their practical usage. As a result, haze and fog removal is essential for an assortment of applications, including satellite imaging and surveillance. The proposed method is intended to remove both weather conditions (haze and fog) in order to restore the final dehazed and defogged outdoor images.

Dehazing/defogging is important for automated parking systems because it produces clear images for identifying pedestrians and vehicles. This is necessary in marine monitoring systems to generate contrast-enhanced images for ship identification. Numerous geographic monitoring methods, such as resource surveys, environmental monitoring, agricultural production and disaster analysis, have become increasingly challenging when haze influences the visibility of remote sensing images. Satellite image quantity and quality are enhanced rapidly, so the images apply to many aspects, e.g., marine monitoring, agricultural production, and geographic information acquisition. The amount of illumination at the specified scene is reduced by bad

**Table 4**

Quantitative evaluation of DHQI and FADE metrics.

Metrics	Images	Xie et al. [31]	Xu et al. [33]	Berman et al. [10]	Shen et al. [59]	Ju et al. [60]	Han et al. [61]	Proposed
DHQI	Fig. 12	60.697	66.880	68.589	62.304	57.183	68.516	68.604
	Fig. 13	50.145	52.345	59.343	62.004	55.039	64.534	64.578
FADE	Fig. 12	0.479	0.232	0.170	0.560	0.195	0.145	0.142
	Fig. 13	0.292	0.426	0.174	0.259	0.311	0.217	0.171

**Table 5**

Comparison of assessment results using statistical measures.

Original image	Statistical Parameters	Gibson et al. [73]	Song et al. [71]	Fattal [5]	He et al. [4]	Berman et al. [10]	Proposed method
House	CC	1.758	1.671	1.236	1.127	1.088	1.764
	e	0.04	0.09	0.14	0.11	0.11	0.10
	r	2.21	1.45	1.48	1.23	1.41	2.23
Pumpkin	CC	1.685	1.561	1.650	1.512	1.812	1.674
	e	0.37	0.26	0.18	0.29	0.24	0.36
	r	3.43	1.57	1.90	1.62	1.98	3.43

weather. Lighting that is inadequate makes an image less visible, making it unsuitable for use in future vision applications including lane detecting systems, radar tracking systems, and weather forecasting. The performance of vision applications in bad weather can therefore be improved using the proposed method.

## 8. Conclusion

As adverse weather is relatively common in remote sensing images, the results of the analysis that follows are impacted. A robust dehazing approach should preserve the integrity of the information in the haze-free area while recovering the information concealed by the haze. This work proposed a novel method to reduce haze and fog in images that were driven by enhancement-based strategies. It comprises the following stages to restore the radiance of the scene: To determine the contrast and color of the images, atmospheric light assessment must appear first. When the atmospheric light is right, the highest intensity values are determined. The estimation of the transmission map using the dark channel prior is then performed to precisely estimate the depth from object to object. Halo artifacts and structural errors can be seen in the final image. The transmission map is optimized by a guided filter method based on unsharp masking to address this problem. The reconstruction of the remote sensing deweathering image is the final step. The outcomes of the experiments show that the prescribed approach works effectively in eradicating bad weather conditions and preserving details, in contrast to prior dehazing strategies.

## CRediT authorship contribution statement

**Apurva Kumari:** Conceptualization, Methodology/Studyc design, Software, Validation, Formal analysis, Investigation, Resources, Data curation, Writing – original draft, Writing – review & editing, Visualization, Project administration. **Subhendu Kumar Sahoo:** Software, Validation, Investigation, Resources, Writing – original draft, Writing – review & editing, Visualization, Supervision, Project administration.

## Declaration of competing interest

The authors declare the following financial interests/personal relationships which may be considered as potential competing interests: APURVA KUMARI reports administrative support and travel were provided by Padmasri Dr BV Raju Institute of Technology. APURVA KUMARI reports a relationship with Padmasri Dr BV Raju Institute of Technology that includes: employment and non-financial support. APURVA KUMARI SINGH has patent pending to Licensee. NO

## Data availability

Data will be made available on request.

## References

- P. Duan, J. Lai, J. Kang, X. Kang, P. Ghamisi, S. Li, Texture-aware total variation-based removal of sun glint in hyperspectral images, *ISPRS J. Photogramm. Remote Sens.* 166 (2020) 359–372.
- L. Jiao, C. Hu, L. Huo, P. Tang, Guided-Pix2Pix: End-to-end inference and refinement network for image dehazing, *IEEE J. Sel. Top. Appl. Earth Obs. Remote Sens.* 14 (2021) 3052–3069.
- P. Duan, P. Ghamisi, X. Kang, B. Rasti, S. Li, R. Gloaguen, Fusion of dual spatial information for hyperspectral image classification, *IEEE Trans. Geosci. Remote Sens.* 59 (9) (2020) 7726–7738.
- K. He, J. Sun, X. Tang, Single image haze removal using dark channel prior, *IEEE Trans. Pattern Anal. Mach. Intell.* 33 (12) (2010) 2341–2353.
- R. Fattal, Single image dehazing, *ACM Trans. Graph.* 27 (3) (2008) 1–9.
- D. Berman, S. Avidan, Non-local image dehazing, in: Proceedings of the IEEE Conference on CVPR, 2016, pp. 1674–1682.
- L. He, J. Zhao, N. Zheng, D. Bi, Haze removal using the difference-structure-preservation prior, *IEEE Trans. Image Process.* 26 (3) (2017) 1063–1075.
- Y. Song, J. Li, X. Wang, X. Chen, Single image dehazing using ranking convolutional neural network, *IEEE Trans. Multimed.* 20 (6) (2018) 1548–1560.
- R.T. Tan, Visibility in bad weather from a single image, in: 2008 IEEE Conference on Computer Vision and Pattern Recognition, IEEE, 2008, pp. 1–8.
- D. Berman, T. Treibitz, S. Avidan, Single image dehazing using haze-lines, *IEEE Trans. Pattern Anal. Mach. Intell.* 42 (3) (2018) 720–734.
- E. Hadjidemetriou, Use of Histograms for Recognition, Columbia University, 2002.
- E.H. Land, J.J. McCann, Lightness and retinex theory, *Josa* 61 (1) (1971) 1–11.
- M.J. Seow, V.K. Asari, Ratio rule and homomorphic filter for enhancement of digital colour image, *Neurocomputing* 69 (7–9) (2006) 954–958.
- Y. Du, B. Guindon, J. Cihlar, Haze detection and removal in high resolution satellite image with wavelet analysis, *IEEE Trans. Geosci. Remote Sens.* 40 (1) (2002) 210–217.
- H.D. Cheng, X.J. Shi, A simple and effective histogram equalization approach to image enhancement, *Digit. Signal Process.* 14 (2) (2004) 158–170.
- T.K. Kim, J.K. Paik, B.S. Kang, Contrast enhancement system using spatially adaptive histogram equalization with temporal filtering, *IEEE Trans. Consum. Electron.* 44 (1) (1998) 82–87.
- J.Y. Kim, L.S. Kim, S.H. Hwang, An advanced contrast enhancement using partially overlapped sub-block histogram equalization, *IEEE Trans. Circuits Syst. Video Technol.* 11 (4) (2001) 475–484.
- W. Shi, J. Li, Research on remote sensing image dehazing algorithm, *Spacecr. Recovery Remote Sens.* 6 (2010) 50–55.
- S. Huang, Y. Liu, Y. Wang, Z. Wang, J. Guo, A new haze removal algorithm for single urban remote sensing image, *IEEE Access* 8 (2020) 100870–100889.
- A.M. Chaudhry, M.M. Riaz, A. Ghafoor, A framework for outdoor RGB image enhancement and dehazing, *IEEE Geosci. Remote Sens. Lett.* 15 (6) (2018) 932–936.
- S. Wang, H. Wan, L. Zeng, X. Peng, Remote sensing image fog removal technology using DCP, *J. Geomat. Sci. Technol.* 3 (2011) 182–185.
- X. Zheng, Y. Xiao, Y. Gong, Research on remote sensing image defogging method based on DCP, *Geomat. Spat. Inf. Technol.* 249 (2020) 69–72.
- L. Li, X. Tang, W. Liu, C. Chen, Speed improvement of aerial image defogging algorithm based on DCP, *J. Jilin Univ.* 59 (2021) 77–84.
- L. Wang, W. Xie, J. Pei, Patch-based dark channel prior dehazing for RS multi-spectral image, *Chin. J. Electron.* 24 (3) (2015) 573–578.
- S. Dai, W. Xu, Y. Piao, Y. Chen, Remote sensing image defogging based on dark channel prior, *Acta Opt. Sin.* 37 (3) (2017) 348–354.

- [26] J.A. Hartigan, M.A. Wong, K-means clustering algorithm, *Appl. Stat.* 28 (1979) 100–108.
- [27] Q. Zhu, J. Mai, L. Shao, A fast single image haze removal algorithm using color attenuation prior, *IEEE Trans. Image Process.* 24 (11) (2015) 3522–3533.
- [28] Q. Liu, X. Gao, L. He, W. Lu, Haze removal for a single visible remote sensing image, *Signal Process.* 137 (2017) 33–43.
- [29] X. Pan, F. Xie, Z. Jiang, J. Yin, Haze removal for a single remote sensing image based on deformed haze imaging model, *IEEE Signal Process. Lett.* 22 (10) (2015) 1806–1810.
- [30] J. Long, Z. Shi, W. Tang, C. Zhang, Single remote sensing image dehazing, *IEEE Geosci. Remote Sens. Lett.* 11 (1) (2013) 59–63.
- [31] F. Xie, J. Chen, X. Pan, Z. Jiang, Adaptive haze removal for single remote sensing image, *IEEE Access* 6 (2018) 67982–67991.
- [32] Q. Guo, H.M. Hu, B. Li, Haze and thin cloud removal using elliptical boundary prior for remote sensing image, *IEEE Trans. Geosci. Remote Sens.* 57 (11) (2019) 9124–9137.
- [33] L. Xu, D. Zhao, Y. Yan, S. Kwong, J. Chen, L.Y. Duan, IDERs: Iterative dehazing method for single remote sensing image, *Inform. Sci.* 489 (2019) 50–62.
- [34] H. Jiang, N. Lu, L. Yao, X. Zhang, Single image dehazing for visible remote sensing based on tagged haze thickness maps, *Remote Sens. Lett.* 9 (7) (2018) 627–635.
- [35] Z. Zhu, H. Wei, G. Hu, Y. Li, G. Qi, N. Mazur, A novel fast single image dehazing algorithm based on artificial multiexposure image fusion, *IEEE Trans. Instrum. Meas.* 70 (2020) 1–23.
- [36] Y. Zheng, J. Zhan, S. He, J. Dong, Y. Du, Curricular contrastive regularization for physics-aware single image dehazing, in: Proceedings of the IEEE/CVF Conference on Computer Vision and Pattern Recognition, 2023, pp. 5785–5794.
- [37] Y. LeCun, Generalization and network design strategies, *Connect. Perspect.* 19 (143–155) (1989) 18.
- [38] Y. LeCun, B. Boser, J.S. Denker, D. Henderson, R.E. Howard, W. Hubbard, L.D. Jackel, Backpropagation applied to handwritten zip code recognition, *Neural Comput.* 1 (4) (1989) 541–551.
- [39] Y. LeCun, L. Bottou, Y. Bengio, P. Haffner, Gradient-based learning applied to document recognition, *Proc. IEEE* 86 (11) (1998) 2278–2324.
- [40] J. Bouvrie, Notes on Convolutional Neural Networks; Neural Nets, MIT CBCL Tech Report, MIT, Cambridge, MA, USA, 2006.
- [41] A. Krizhevsky, I. Sutskever, G.E. Hinton, Imagenet classification with deep convolutional neural networks, *Commun. ACM* 60 (6) (2017) 84–90.
- [42] B. Cai, X. Xu, K. Jia, C. Qing, D. Tao, Dehazenet: An end-to-end system for single image haze removal, *IEEE Trans. Image Process.* 25 (11) (2016) 5187–5198.
- [43] W. Ren, J. Pan, H. Zhang, X. Cao, M.H. Yang, Single image dehazing via multi-scale convolutional neural networks with holistic edges, *Int. J. Comput. Vis.* 128 (1) (2020) 240–259.
- [44] B. Li, X. Peng, Z. Wang, J. Xu, D. Feng, Aod-net: All-in-one dehazing network, in: Proceedings of the IEEE International Conference on Computer Vision, 2017, pp. 4770–4778.
- [45] D. Chen, M. He, Q. Fan, J. Liao, L. Zhang, D. Hou, G. Hua, Gated context aggregation network for image dehazing and deraining, in: 2019 IEEE (WACV), 2019, pp. 1375–1383.
- [46] S. Salazar-Colores, I. Cruz-Aceves, J.M. Ramos-Arreguin, Single image dehazing using a multilayer perceptron, *J. Electron. Imaging* 27 (4) (2018) 043022.
- [47] J. Shin, M. Kim, J. Paik, S. Lee, Radiance-reflectance combined optimization and structure-guided  $\ell_0$ -norm for single image dehazing, *IEEE Trans. Multimed.* 22 (1) (2019) 30–44.
- [48] M. Qin, F. Xie, W. Li, Z. Shi, H. Zhang, Dehazing for multispectral remote sensing images based on a convolutional neural network with the residual architecture, *IEEE J. Sel. Top. Appl. Earth Obs. Remote. Sens.* 11 (5) (2018) 1645–1655.
- [49] X. Liu, H. Li, C. Zhu, Joint contrast enhancement and exposure fusion for real-world image dehazing, *IEEE Trans. Multimed.* 24 (2021) 3934–3946.
- [50] B.P. Kumar, A. Kumar, R. Pandey, Region-based adaptive single image dehazing, detail enhancement and pre-processing using auto-colour transfer method, *Signal Process., Image Commun.* 100 (2022) 116532.
- [51] D. Lin, G. Xu, X. Wang, Y. Wang, X. Sun, K. Fu, A remote sensing image dataset for cloud removal, 2019.
- [52] B. Huang, L. Zhi, C. Yang, F. Sun, Y. Song, Single satellite optical imagery dehazing using SAR image prior based on conditional generative adversarial networks, in: Proceedings of the IEEE/CVF Winter Conference on Computer Vision, 2020, pp. 1806–1813.
- [53] G.S. Xia, J. Hu, F. Hu, B. Shi, X. Bai, Y. Zhong, et al., AID: A benchmark data set for performance evaluation of aerial scene classification, *IEEE Trans. Geosci. Remote Sens.* 55 (7) (2017) 3965–3981.
- [54] Y. Bie, S. Yang, Y. Huang, Single remote sensing image dehazing using Gaussian and physics-guided process, *IEEE Geosci. Remote Sens. Lett.* 19 (2022) 1–5.
- [55] A. Mehta, H. Sinha, M. Mandal, P. Narang, Domain-aware unsupervised hyperspectral reconstruction for aerial image dehazing, in: Proceedings of the IEEE/CVF Winter Conference on Applications of Computer Vision, 2021, pp. 413–422.
- [56] Z. He, C. Gong, Y. Hu, L. Li, Remote sensing image dehazing based on an attention convolutional neural network, *IEEE Access* 10 (2022) 68731–68739.
- [57] H. Li, Y. Zhang, J. Liu, et al., GTMNet: a vision transformer with guided transmission map for single remote sensing image dehazing, *Sci. Rep.* 13 (9222) (2023).
- [58] Z. Chen, Q. Li, H. Feng, Z. Xu, Y. Chen, Nonuniformly dehaze network for visible remote sensing images, in: Proceedings of the IEEE/CVF Conference on Computer Vision and Pattern Recognition, 2022, pp. 447–456.
- [59] H. Shen, C. Zhang, H. Li, Q. Yuan, L. Zhang, A spatial-spectral adaptive haze removal method for visible remote sensing images, *IEEE Trans. Geosci. Remote Sens.* 58 (9) (2020) 6168–6180.
- [60] M. Ju, C. Ding, W. Ren, Y. Yang, D. Zhang, Y.J. Guo, IDE: Image dehazing and exposure using an enhanced atmospheric scattering model, *IEEE Trans. Image Process.* 30 (2021) 2180–2192.
- [61] J. Han, S. Zhang, N. Fan, Z. Ye, Local patchwise minimal and maximal values prior for single optical remote sensing image dehazing, *Inform. Sci.* 606 (2022) 173–193.
- [62] L.K. Choi, J. You, A.C. Bovik, Referenceless prediction of perceptual fog density and perceptual image defogging, *IEEE Trans. Image Process.* 24 (11) (2015) 3888–3901.
- [63] X. Min, G. Zhai, K. Gu, X. Yang, X. Guan, Objective quality evaluation of dehazed images, *IEEE Trans. Intell. Transp. Syst.* 20 (8) (2018) 2879–2892.
- [64] J. Pan, J. Dong, Y. Liu, J. Zhang, J. Ren, J. Tang, Y.W. Tai, M.H. Yang, Physics-based generative adversarial models for image restoration and beyond, *IEEE Trans. Pattern Anal. Mach. Intell.* 43 (7) (2021) 2449–2462.
- [65] N.H. Kaplan, Real-world image dehazing with improved joint enhancement and exposure fusion, *J. Vis. Commun. Image Represent.* 90 (2023) 103720.
- [66] Y.B. Özçelik, A. Altan, Overcoming nonlinear dynamics in diabetic retinopathy classification: A robust AI-based model with chaotic swarm intelligence optimization and recurrent long short-term memory, *Fractal Fract.* 7 (8) (2023) 598.
- [67] İ. Yağ, A. Altan, Artificial intelligence-based robust hybrid algorithm design and implementation for real-time detection of plant diseases in agricultural environments, *Biology* 11 (12) (2022) 1732.
- [68] A. Sezer, A. Altan, Detection of solder paste defects with an optimization-based deep learning model using image processing techniques, *Solder. Surf. Mount Technol.* 33 (5) (2021) 291–298.
- [69] Z. Wang, A.C. Bovik, H.R. Sheikh, E.P. Simoncelli, Image quality assessment: from error visibility to structural similarity, *IEEE Trans. Image Process.* 13 (4) (2004) 600–612.
- [70] N. Hautiere, J.P. Tarel, D. Aubert, E. Dumont, Blind contrast enhancement assessment by gradient ratioing at visible edges, *Image Anal. Stereol.* 27 (2) (2008) 87–95.
- [71] Y. Song, H. Luo, R. Lu, J. Ma, Dehazed image quality assessment by haze-line theory, *J. Phys. Conf. Ser.* 844 (1) (2017) 012045.
- [72] P. Dong, B. Wang, TransRA: Transformer and residual attention fusion for single remote sensing image dehazing, *Multidimens. Syst. Signal Process.* 33 (4) (2022) 1119–1138.
- [73] K.B. Gibson, T.Q. Nguyen, Fast single image fog removal using the adaptive Wiener filter, in: 2013 IEEE International Conference on Image Processing, IEEE, 2013, pp. 714–718.